3D PRINTING OF NANOANTENNA ARRAYS FOR OPTICAL METASURFACES

by

Jithin Prabha

A Thesis

Submitted to the Faculty of Purdue University

In Partial Fulfillment of the Requirements for the degree of

Master of Science in Mechanical Engineering

School of Mechanical Engineering

West Lafayette, Indiana

December 2018

THE PURDUE UNIVERSITY GRADUATE SCHOOL
STATEMENT OF COMMITTEE APPROVAL

Dr. Xianfan Xu, Chair

School of Mechanical Engineering

Dr. Liang Pan

School of Mechanical Engineering

Dr. Bryan Boudouris

Davidson School of Chemical Engineering

Approved by:

Dr. Jay P. Gore

Head of the Graduate Program

To Achan, Amma
and Nonan

ACKNOWLEDGEMENTS

First of all, I would like to thank my advisor, Dr. Xianfan Xu for his support and guidance throughout my graduate study. Prof. Xu always encouraged me to go step by step to solve the challenges that I came across in this work and to always look at the fundamentals. I would also like to thank my committee members Dr. Bryan Boudouris and Dr. Liang Pan for being part of my committee and for the valuable discussions.

I would like to thank Xiaolong He for introducing me to the system and Paul Somers for all the help and support that he gave me throughout the study. I would like to thank Teng Chi, Shih-Hsin Hsu and Dr. Sanjoy Mukherjee for all the help and support. I would like to thank Shouyuan Huang, and Prabhu Kumar Venuthurumilli for helping with the e-beam evaporation process and also for valuable discussions. I would like to thank Vasudavan Iyer and Hakan Salihoglu for help with the FTIR and for valuable discussions. I would like to thank Dr. Anurup Datta for helping me understand the simulation software. I would like to thank Peter Barton for all the help with understanding silver printing and helping with the SEM. I would like to thank all members of the research group for all their help and support without which this work would not have been possible.

I would like to thank all my friends for their support and especially Athul, Varun and Mable for being my family at Purdue. Last but not least I would like to thank my family for always being with me.

TABLE OF CONTENTS

LIST OF FIGURES vi
ABSTRACT x
1. INTRODUCTION 1
1.1 Background Information 1
1.2 Free Radical Photopolymerization 4
1.3 Applications of Two Photon Fabrication 7
1.4 Outline of Thesis 9
2. EXPERIMENTAL 10
2.1 Experimental Setup 10
2.2 Synthesis of Photoresist 13
2.3 Scanning Procedure 14
2.4 3D Printed Structures 17
2.5 Summary 21
3. NANOANTENNAS 22
3.1 Introduction 22
3.2 Diabolo Antenna Arrays by 3D Printing 24
3.3 Simulation of Optical response of the Nanostructure Array 31
3.4 FTIR Reflectance Measurement 31
3.5 Summary 32
4. CONCLUSIONS AND FUTURE WORK 43
4.1 Summary and Conclusions 43
4.2 Future Work 44
REFERENCES 46
PUBLICATION 48

LIST OF FIGURES

Figure 1.1: UV light and ultrashort pulses through a dye to show non-linear interaction in the second case. [3]……....1

Figure 1.2: (a) Linear excitation vs two photon excitation (b) Spatial intensity profiles in the center of the beam axis for the two cases. The profile of excited molecules integrated in the transverse direction is shown at the left of each 3D plot [1]…….…….3

Figure 1.3: Schematic showing printing of the 3D structure inside the resin…..……3

Figure 1.4: Acrylate functionality and Methacrylate functionality [1]……4

Figure 1.5: (a) PETA, (b) PETTA [1]……..4

Figure 1.6: (a) Micro-bull structure [7] (b) functional micro-oscillator system scale bar is 2 µm…. ……..7

Figure 1.7: (a) Sections of microvalves for microfluidics[8] (b) Micro-caged device for drug delivery [9] (c) An example of a metamaterial - ultrastiff ultralight micro-lattice [10] (d) electrostatically tunable plasmonic device using high order diffraction modes on multi-photon polymerized three-dimensional micro-springs [11] ……8

Figure 2.1: Schematic of setup……...10

Figure 2.2: Coherent Micra10 femtosecond laser……..…...…….……11

Figure 2.3: EOM……12

Figure 2.4: Galvo mirror……....12

Figure 2.5: Inverted microscope……....12

Figure 2.6: Chemicals used: (a) ZPO, (b) MAPTMS, (c) DMAEMA, (d) MAA, (e) BIS [4]…..13

Figure 2.7: (a) CAD model of the truss bridge, (b) slicing, (c) SEM image of printed structure laser power 4mW, scan speed 200µm/s, 400nm layers…..……..……..15

Figure 2.8: (a) SEM image (top view) of a triangle structure formed by conventional scanning, (b) beam path used for (a), (c) SEM image (top view) of a triangular structure formed by overscanning procedure, (d) overscanning pattern – the laser beam is on only inside the triangle, both the structures are made using 20µm/s scan speed, 3.6mW laser power and 100 nm layer height……...……..16

Figure 2.9: (a)Top view and (b) tilted view of printed structure with (c) CAD model…….17

Figure 2.10: (a)Top view and (b) tilted view of printed structure with (c) CAD model……...18

Figure 2.11: (a)Top view and (b) tilted view of printed structure with (c) CAD model……... 18
Figure 2.12: (a)Top view and (b) tilted view of printed structure with (c) CAD model……... 19
Figure 2.13: Woodpile structure fabricated using photoresist without quencher showing line width of 350 nm, laser power 2.8mW,scan speed 20µm/s……..…….. 20
Figure 2.14: Woodpile structure fabricated using photoresist without quencher showing line width of 120 nm, laser power 2.8mW, scan speed 20µm/s…….…….. 20
Figure 3.1: Bowtie shaped structures with the correct polarization of excitation shown by the black arrows (a) bowtie antenna - BA, (b) bowtie aperture antenna - BAA, (c) diabolo antenna - DA, (d) complementary bowtie aperture CBA ... .…… 22
Figure 3.2: (a) Simulation model for diabolo antenna showing gold structure of thickness T on glass, other dimensions as shown and electric field polarization direction, (b) Magnetic field enhancement (G = T = 50 nm, D = 310 nm, λ = 1940 nm) excited result showing central hotspot with peak magnetic field enhancement of 220 normalized with the magnetic field without the gold structure [12] ……..23
Figure 3.3: (a) The top view of the cad model of the diabolo antenna with dimensions, (b) shows the tilted view of the antenna with a height of 400nm, (c) The conventional scan pattern for a layer, (d) shows the over-scan pattern for the layer, the red lines indicate that the laser ison…….…….…… 24
Figure 3.4 SEM image of printed diabolo antenna showing dimensions (top view)…….25
Figure 3.5: SEM image of tilted view of printed diabolo antenna…….25
Figure 3.6: (a) Top view and (b) tilted view of diabolo antenna after resolving bridge height issue……..……..26
Figure 3.7: Diabolo antenna written at different parameters of laser power 3mW, writing speed 10µm/s, 100nm layer height and total height 400nm……..…… 27
Figure 3.8: The tip-tilt stage (i) mounted on top of the piezo stage(ii), the pitch and roll adjustment knobs are seen on the left side of (i). Sample is mounted on (i)……. 27
Figure 3.9: (a)Top view of a 40µm square array with a 10×10 pattern with periodicity in the x & y direction of 4µm each, the array is coated with 55µm of gold, (b) tilted view of the same structure, writing parameters power – 3.8mW, scan speed - 40µm/s and layer height - 100nm ……. 28
Figure 3.10: (a) Close up of the top view of the array showing 4 antennas, (b) close up view

of the tilted array, (c) top view of single antenna, (d) tilted view of single antenna showing layers of the gold layer on glass forming BAA (i), polymer layer (ii) and gold coating on antenna……. 29
Figure 3.11:The BAA (i), the Diabolo Antenna (DA) (iii) and polymer (ii) ……29
Figure 3.12:The geometry for simulation showing the various parameters that are involved….. 31
Figure 3.13: Reflectance plot for optimized structure showing reflectance dip at 4.04 µm……..32
Figure 3.14: Varying the height (h) of the antenna showing reflectance drop to zero for 0.4 µm height……..33
Figure 3.15:Varying length of bowtie (bl) showing zero reflection for bl = 2.6 µm…….33
Figure 3.16:Varying bowtie width (bw) showing zero reflection for bw = 2µm……..…… 34
Figure 3.17:Varying neck length (nl) shows that it does not have a large impact and chose optimum nl = 0.6 µm……. 34
Figure 3.18: Varying neck width (nw) shows that it does not have a large impact and chose optimum nw=0.3µm…..……..…… 35
Figure 3.19: Varying gold thickness (t) shows that it does not have a large impact and optimum t is chosen as 55nm……...……..……35
Figure 3.20: (a) Magnetic field on antenna and aperture at resonance condition of 4.04 µm, (b) magnetic field on antenna and aperture at off resonance condition of 4.35 µm……36
Figure 3.21: (a) Magnetic field on antenna and aperture at resonance condition of 4.04 µm, (b) magnetic field on antenna and aperture at off resonance condition of 4.35 µm……36
Figure 3.22: (a) Current density plot at resonance (b) current density vector plot at resonance... 37
Figure 3.23: the cross-sectional plane (i) at the center of the antenna used to plot the fields….. 37
Figure 3.24: Magnetic field at resonance - the magnetic field hotspots between the aperture and the antenna happens only at resonance condition …….. ……38
Figure 3.25: Magnetic field off resonance…….38
Figure 3.26: Electric field hot spot at resonance……38
Figure 3.27: Electric field off resonance……39
Figure 3.28: Reflectance and transmittance for optimum structure…...……39
Figure 3.29: Calculated absorption in aperture for the incident wave polarization direction shown in fig 3.12 represented as 0 degree and the polarization direction perpendicular to it shown as 90degree…….……..……40

Figure 3.30: FTIR reflectance measurement for incident light polarized along the antenna (0), perpendicular to antenna (90) and at an angle of 135 degrees……...…41

ABSTRACT

Author: Prabha, Jithin. MSME
Institution: Purdue University
Degree Received: December 2018
Title: 3D Printing of Nanoantenna Arrays for Optical Metasurfaces
Committee Chair: Xianfan Xu

Additive manufacturing using 2 photon polymerization is of great interest as it can create nanostructures with feature sizes much below the diffraction limit. It can be called as true 3D printing as it can fabricate in 3 dimensions by moving the laser spot in any 3D pattern inside the resist. This unique property is attributed to the non-linearity of two photon absorption which makes the polymerization happen only at the focal spot of the laser beam. This method has a wide range of applications such as optics/photonics, metamaterials, metasurfaces, micromachines, microfluidics, tissue engineering and drug delivery.

This work focuses on utilizing 2 photon fabrication for creating a metasurface by printing diabolo antenna arrays on a glass substrate and subsequently metallizing it by coating with gold. A femtosecond laser is used along with a galvo-mirror to scan the geometry inside the photoresist to create the antenna. The structure is simulated using ANSYS HFSS to study its properties and optimize the parameters. The calculations show a reflectance dip and zero reflectance for the resonance condition of 4.04 μm. An array of antennas is fabricated using the optimized properties and coated with gold using e-beam evaporation. This array is studied using a fourier transform infrared spectrometer and polarization dependent reflectance dip to 40% is observed at 6.6 μm. The difference might be due to the small errors in fabrication. This method of 3D printing of antenna arrays and metallization by a single step of e-beam evaporation is hence proved as a viable

method for creating optical metasurfaces. Areas of future research for perfecting this method include incorporating an autofocusing system, printing more complicated geometries for antennas, and achieving higher resolution using techniques like stimulated emission depletion.

1. INTRODUCTION

1.1 Background Information

Microfabrication of polymer structures can be done in a variety of methods and among them multiphoton absorption holds a very unique position due to the ability to create very complex three dimensional structures using a single laser beam. The process can be considered as the real 3D printing as the structure can be formed in a truly three-dimensional manner with the 3D scanning of the focal spot compared to other methods of additive manufacturing which are done layer by layer. Two photon absorption based free radical photopolymerization is what enables this remarkable feat.

Two photon absorption is the simultaneous absorption of two photons to increase the energy level of a molecule from one state to a higher excited state. This was proposed by the Nobel prize winning physicist Maria Goeppert-Mayer in 1931 in her doctoral thesis and was then published [2]. This was first experimentally verified 30 years later when the laser was invented. Two photon polymerization is a technique that was invented in the mid 1990's in which two photon absorption is used to create complex micro and nano-structures. In this process, two photon absorption is used to create and initiate photochemical changes in a transparent mixture of monomer and photo-initiator. This will lead to polymerization only at the focal spot. Fig. 1.1 shows the difference between simple UV light focused into a fluorescent dye verses an ultrafast laser focused into it. We can clearly see that due to non-linear laser matter interactions, only the focal spot is illuminated in case of the ultrashort pulses.

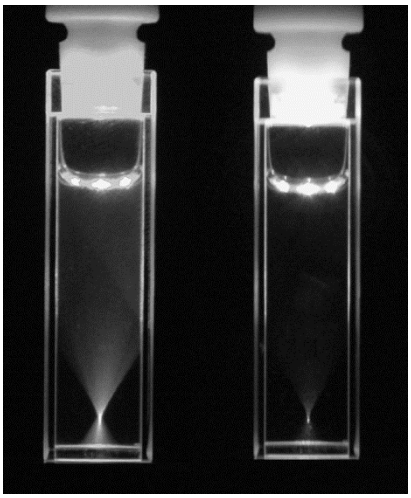

Figure 1.1: UV light and ultrashort pulses through a dye to show non- linear interaction in the second case. [3].

Processes like lithography depend on single photon absorption in which the material response is linear, which can be expressed by the polarization in the medium [1]

$$\boldsymbol{P}(\omega) = \varepsilon_0 \chi(\omega) \boldsymbol{E}(\omega) \tag{1.1}$$

Here, $\boldsymbol{P}$ is the polarization, ω is the angular frequency, ε_0 is the permittivity of free space, χ is the linear susceptibility of the medium and $\boldsymbol{E}$ is the electric field. The absorption coefficient α is proportional to the imaginary part of the susceptibility [1].

$$\alpha(\omega) = \frac{\omega}{cn} \chi_{Im}(\omega) \tag{1.2}$$

here *n* is the refractive index of the medium. The light absorbed by a medium in a linear process is proportional to the product of the absorption coefficient and light intensity. Intensity is proportional to the square of the magnitude of the electric field which makes the light absorbed proportional to $|\boldsymbol{E}|^2 \chi_{Im}(\omega)$ [1].

The response of the medium need not be a linear process, a more general expression for polarization is [1]

$$\boldsymbol{P} = \varepsilon_0 \left(\chi^{(1)} \boldsymbol{E} + \chi^{(2)} \boldsymbol{E} \cdot \boldsymbol{E} + \chi^{(3)} \boldsymbol{E} \cdot \boldsymbol{E} \cdot \boldsymbol{E} + \cdots \right) = \boldsymbol{P}^{(1)} + \boldsymbol{P}^{(2)} + \boldsymbol{P}^{(3)} + \cdots \tag{1.3}$$

here, $\chi^{(n)}$ is the n^{th} order susceptibility. The rate of linear absorption is proportional to $\mathbf{E} \cdot \mathbf{P}^{(1)}$ which is proportional to intensity. Two photon absorption is proportional to the square of the intensity, so it is proportional to $\mathbf{E} \cdot \mathbf{P}^{(3)}$ which involves four optical fields.

In two photon absorption the first photon excites the molecule into a virtual and the second photon takes it to the upper level (Fig 1.2 (a)). In case of the laser beam the two photons absorbed are of the same frequency and the energy difference between the two states is provided by the sum of the two photons. In case of the laser used in the experiments, the 800nm femtosecond laser allows the excitation that a 400nm continuous wave provides (single photon absorption), but using the two photon absorption process. The non-linearity of this process enables writing the 3D structures.

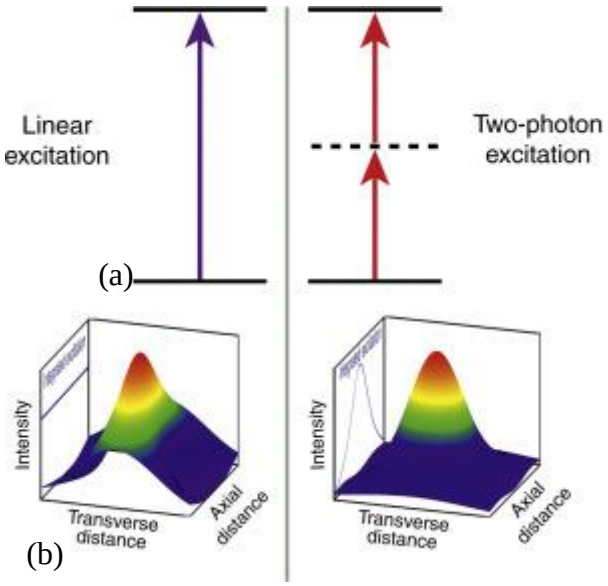

Figure 1.2: (a) linear excitation vs two photon excitation (b) Spatial intensity profiles in the center of the beam axis for the two cases. The profile of excited molecules integrated in the transverse direction is shown at the left of each 3D plot [1].

The process of fabrication is shown in the schematic shown in Fig 1.3. The laser is focused onto the photopolymerizable resin as shown in the figure by an objective lens and the focal spot is moved in the required pattern to form the 3D structure.

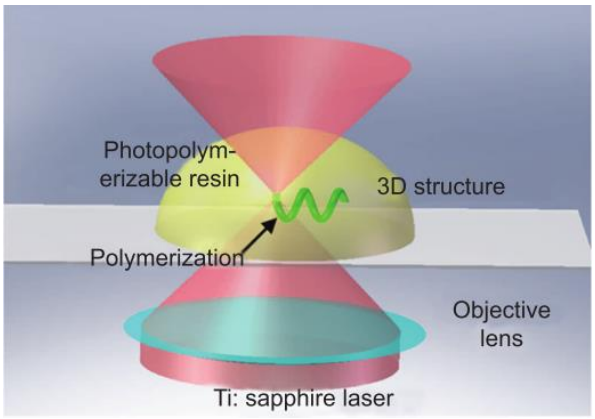

Figure 1.3: Schematic showing printing of the 3D structure inside the resin [5].

The mechanism behind the polymerization is called free radical photopolymerization and is explained in the next subsection.

1.2 Free Radical Photopolymerization

The chemical mechanism behind the process is called free radical photopolymerization. The monomers that are used widely are acrylates and methacrylates. Their characteristics vary, methacrylates are better at making 3D structures because polymethacrylates are stiffer with a higher tensile strength and lower elongation, this is a result of the steric hindrance due to the additional methyl group of the methacrylate. The vinyl group (−CH=CH2) present in the structure which can be seen at the ends of the chains of both PETA and PETTA in Fig 1.5, reacts readily in the presence of radicals and it is this mechanism that drives the 2-photon polymerization reaction. Some examples of acrylates are pentaerythritol triacrylate (PETA) and pentaerythritol tetraacrylate (PETTA) and an example of methacrylate is 2-(dimethylamino)ethyl methacrylate (DMAEMA)[1].

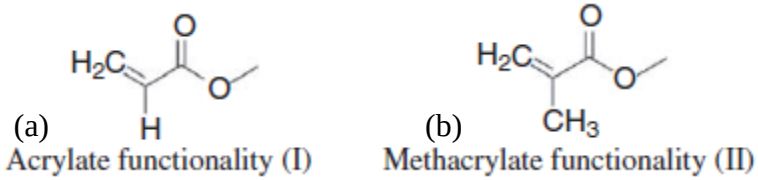

Figure 1.4: Acrylate functionality and Methacrylate functionality [1].

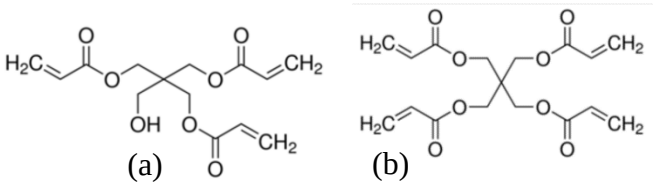

Figure 1.5: (a) PETA, (b) PETTA [1].

Polymerization Steps

The photopolymerization reaction involves a multiple of steps namely initiation, propagation, chain transfer and the termination steps that involve primary termination, bimolecular termination and monomolecular termination, these reactions are shown below.

Initiation step - primary radicals (In•, the dot represents an unpaired electron) are formed from light interactions (rate constant k_d) and they add to monomer molecules with a rate constant k_i. k_i is usually much higher than k_d, which implies that radical formation is the rate-determining step for the initiation.

Propagation - is the growth of the polymer chain and more monomer molecules get added up. Rate can be expressed as $R_p = k_p [M] [P^{\bullet}]$ where [M] is monomer concentration and $[P^{\bullet}]$ is the total reactive radical concentration. In the following equations, In represents the radical, • represents an unpaired electron, M represents monomer, M_n represents a growing chain, R is a small molecule that the growing chain encounters, all k's represent the rate constants.

$$In \xrightarrow{k_d} In\bullet \qquad \text{initiation} \qquad (1.4)$$

$$In\bullet + M \xrightarrow{k_i} {\sim}M_1\bullet \qquad \text{initiation} \qquad (1.5)$$

$${\sim}M_n\bullet + M \xrightarrow{k_p} {\sim}M_{n+1}\bullet \qquad \text{propagation} \qquad (1.6)$$

$${\sim}M_n\bullet + RH \xrightarrow{k_{tr}} {\sim}M_nH + R\bullet \qquad \text{chain transfer} \qquad (1.7)$$

$${\sim}M_n\bullet + In\bullet \xrightarrow{k_t^p} dead\ polymer \qquad \text{primary termination} \qquad (1.8)$$

$${\sim}M_n\bullet + {\sim}M_m\bullet \xrightarrow{k_t^b} dead\ polymer \qquad \text{bimolecular termination} \qquad (1.9)$$

$${\sim}M_n\bullet \xrightarrow{k_t^m} ({\sim}M_n\bullet)_{trapped} \qquad \text{monomolecular termination} \qquad (1.10)$$

Chain transfer – is a side reaction which happens to the polymer in which the polymerization stops, and the radical is transferred to R.

Termination – In this step, the radicals are destroyed, and further polymerization is stopped, it can occur by 3 different pathways.

a. Primary termination – The growing polymer chain encounters a primary radical and hence the reaction stops. This happens at very high primary radical formation like in the case when the photoinitiator concentration is very high or in the case of a high light intensity.
b. Bimolecular termination – This happens when two macroradicals ($M_n^{\bullet}$) react with each other. It is dominant when there is no added inhibitor or agents.

$$R_t^b = -\frac{dP\bullet}{dt} = 2 \cdot k_t^b \cdot [P\bullet]^2 \quad (1.11)$$

c. Monomolecular termination – this is the mechanism in which the radicals are trapped because of a decrease in mobility.

$$R_t^m = -\frac{dP\bullet}{dt} = k_t^m \cdot [P\bullet] \quad (1.12)$$

The overall rate of polymerization under the assumption of steady state and exclusively bimolecular termination can be expressed as

$$R_p = k_p \cdot [M] \cdot \left(\frac{R_i}{2 \cdot k_t^b}\right)^{0.5} \quad (1.13)$$

Where Ri is the initiation rate [1].

1.3 Applications of Two Photon Fabrication

In 1997, Maruo et al. [6] published the paper that invented the application of two photon polymerization for microfabrication. They were able to get a feature size of 1.3 μm using a Ti:Sapphire laser of 780 nm with 200 fs pulses and using a UV-photopolymerizable resin. Kawata et al. [7] obtained sub-diffraction feature sizes of 120 nm and the famous micro-bull, shown in Fig 1.6 was fabricated along with a functional micro-oscillator system.

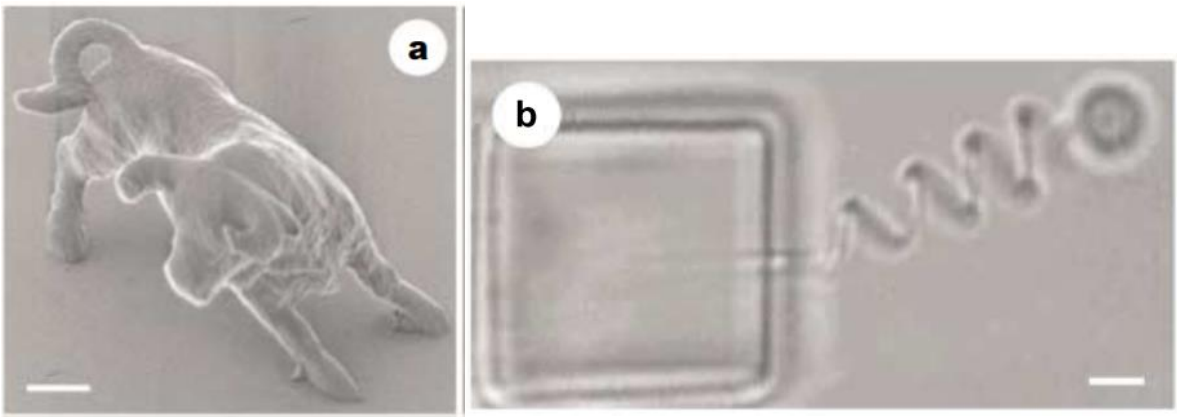

Figure 1.6: (a) micro-bull structure [7] (b) functional microoscillator system scale bar is 2 μm[7].

A wide variety of applications of the process of 3D microfabrication are developed over the years in diverse fields such as optics/photonics, metamaterials, metasurfaces, micromachines, microfluidics, tissue engineering, drug delivery etc. Some examples of the applications can be seen in Fig 1.5. Fig 1.5 (a) shows the cross section of readily assembled micro valves that are fabricated by two photon fabrication for use in micro-fluidics[8]. Fig 1.5 (b) shows a micro-caged device for controlled drug delivery, the cage is filled with the therapeutic agent and implanted into target tissue where it is released through the pores [9]. Fig 1.5 (c) shows a metamaterial micro-lattice that was printed with engineered property of being ultralight and ultrastiff [10].

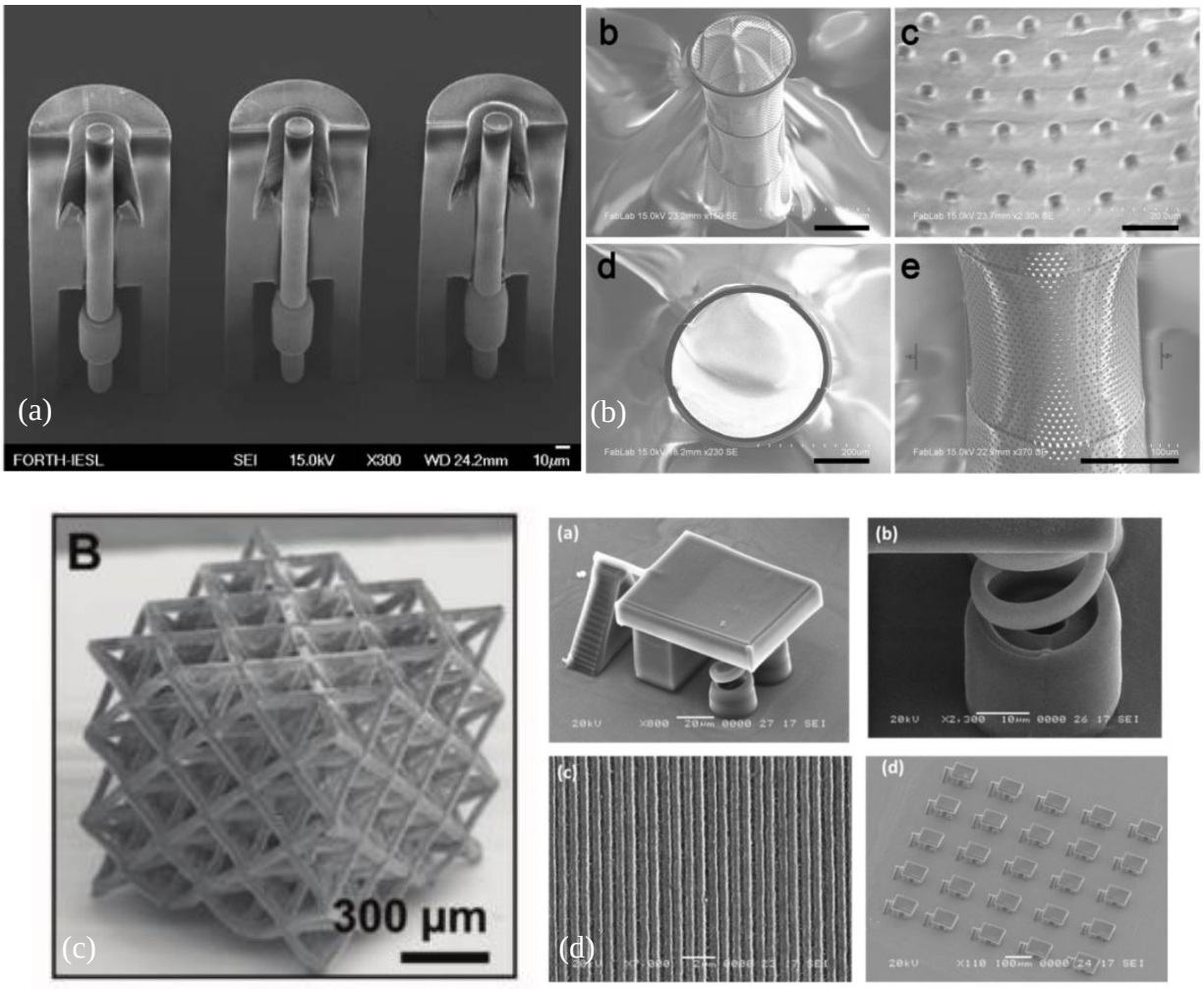

Figure 1.7: (a) Sections of microvalves for microfluidics[8] (b) Micro-caged device for drug delivery [9] (c) An example of a metamaterial - ultrastiff ultralight micro-lattice [10] (d) electrostatically tunable plasmonic device using high order diffraction modes on multi-photon polymerized three-dimensional micro-springs [11].

Fig 1.5 (d) shows a tunable plasmonic device in which the tilt angle of the top plate can be varied by applying a voltage [11]. The array is gold coated by sputtering. The array shows a variation in reflection properties with the voltage applied that is the tilt of the top plate. This thesis focuses on such an application of microfabrication in which an array of nano-antennas is fabricated using two photon polymerization and then is coated with gold which gives it properties like selectively absorbing and transmitting particular frequencies of light.

1.4 Outline of Thesis

In this work, two photon fabrication of nanoantenna arrays is performed using an 800nm femtosecond laser. The arrays are further coated with gold using E-beam evaporation and the reflectivity of the array is measured to obtain its properties. The properties are simulated using ANSYS HFSS. The structures are studied using a scanning electron microscope and a Fourier Transform Infrared Spectrometer (FTIR) is used to measure the reflectance properties. Chapter 2 explains the experimental procedures including the setup and the synthesis of the photoresist and explains the scanning procedure. It also contains the initial 3D printing results. Chapter 3 gives an introduction to nano-antennas, explains the experimental procedure for 3D printing nanoantennas and shows the printing results of antenna arrays. The chapter also explains the simulations and results obtained using ANSYS HFSS. Chapter 4 describes the summary and conclusions that can be made and scopes of future work.

2. EXPERIMENTAL

2.1 Experimental Setup

The experimental setup involves a femtosecond laser, CPC (Compound Parabolic Concentrator-Coherent), Electro-optical modulator (EOM - Physik Instrumente), a tip-tilt galvo-mirror (Physik Instrumente), an inverted microscope (Nikon), a piezoelectric stage to move the sample, and various lenses and mirrors to process the laser beam. The setup and the programs to control were made by the efforts of Dr. Anurup Datta - former student in the group, Paul Somers - PhD student and me. The laser is a mode-locked Coherent Micra-10 femtosecond laser operating at 800 nm central wavelength, 30 fs pulse width and 80 MHz repetition rate which can be seen in figure 2.2.

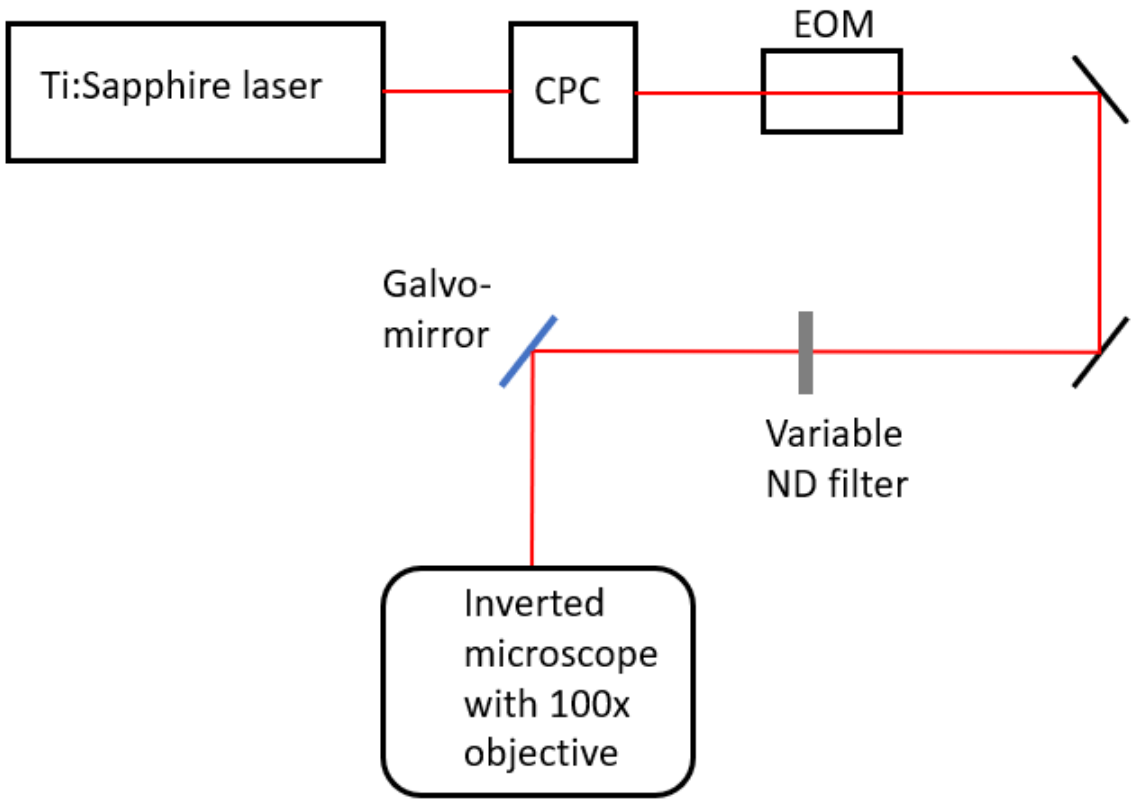

Figure 2.1: Schematic of setup.

The laser passes through the CPC to adjust group velocity dispersion to compensate for the optics used further in the beam path thus keeping the pulse width at the sample location. The beam further passes through the EOM which is used as an amplitude modulator for turning the beam on and off for the writing process. The need for an EOM (Fig 2.3) will be further explained later in the scanning procedure section. The power of the laser beam is controlled by a variable neutral density filter. The laser scanning is made possible by the tip-tilt galvo mirror (Fig 2.4) which makes the fabrication possible. The beam finally hits the sample through a using a 100x oil-immersion objective lens with a numerical aperture of 1.49 (Nikon).

Figure 2.2: Coherent Micra-10 femtosecond laser.

The sample is mounted on a small tip-tilt stage which is further mounted on the piezo stage which helps to move the sample in the x, y and z directions. The lens and the sample are held by the microscope (Fig 2.5) which also has the CCD for viewing. The laser power is measured by a Molectron thermocouple power meter just before the beam enters the microscope. The control of the system is made possible by LabVIEW and Field Programmable Gate Array (FPGA). The EOM, the galvo-mirror and the piezo stage are connected to the computer through the FPGA card. The LabView programs control these elements.

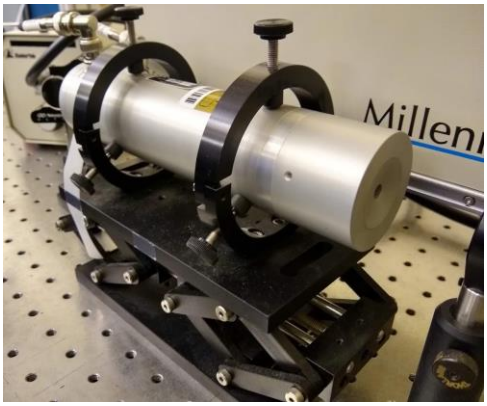

Figure 2.3: EOM.

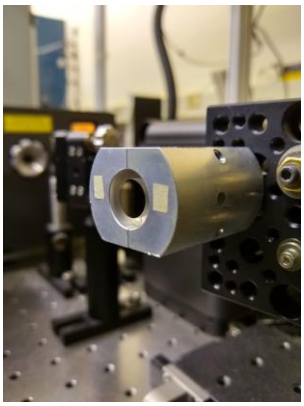

Figure 2.4: Galvo mirror.

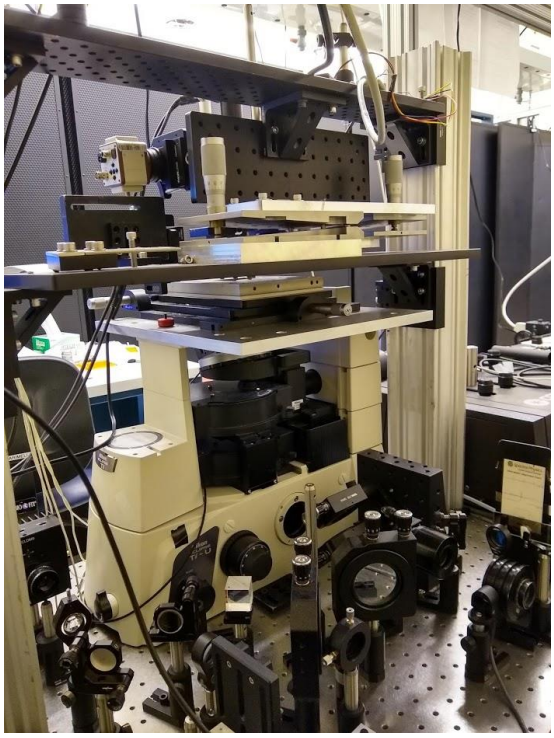

Figure 2.5: Inverted microscope.

For creating 3D structures, the CAD file is first created in a software such as Autodesk Inventor and converted to a .stl format. The CAD file is further processed and sliced into different layers by the Slic3r program, which further gives the GCODE file. This GCODE file is read by the LabVIEW program which controls the scanning process. For fabrication of the nanoantennas

conventional scanning was insufficient and the method of over-scanning was utilized as further described in section 2.3.

2.2 Synthesis of Photoresist

The photoresist was synthesized based on the recipe from Sakellari et al [4] with the quencher also added. The ingredients are zirconium propoxide, (Fig 2.6 (a), ZPO), which helps in the formation of an inorganic matrix backbone, methacryloxypropyl trimethoxysilane, as monomer (Fig 2.6 (b), MAPTMS), 2-(dimethylamino)ethyl methacrylate (Fig 2.6 (c), DMAEMA) as the quencher, methacrylic acid as monomer (Fig 2.6 (d), MAA), and Michler's ketone, 4,4-bis(diethylamino) benzophenone (Fig 2.6 (e) BIS) as the photoinitiator.

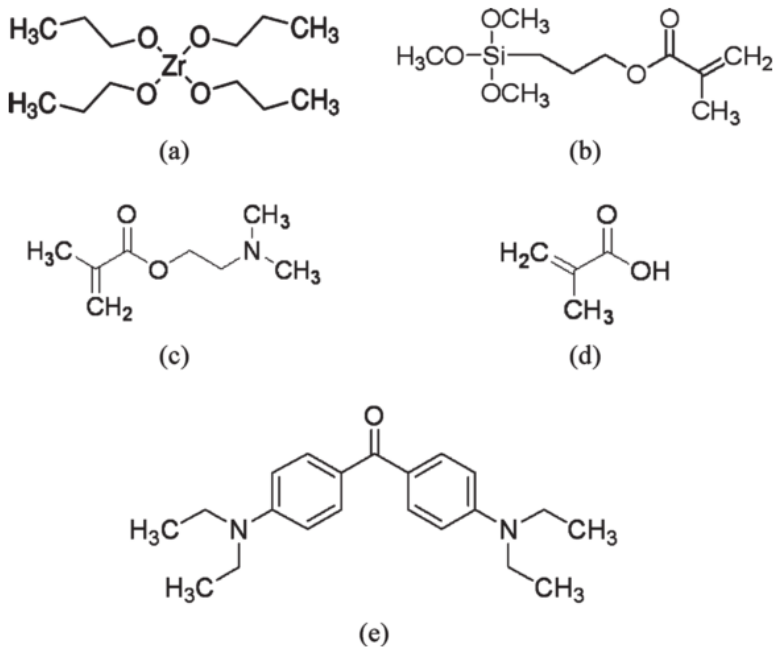

Figure 2.6: Chemicals used: (a) ZPO, (b) MAPTMS, (c) DMAEMA, (d) MAA, (e) BIS [4].

MAPTMS is first hydrolyzed using HCL solution (0.1M) at a 1:0.1mass ratio, these two liquids are not miscible, and two phases are formed. This mixture is stirred until a homogenous clear

solution is formed. In a separate vial, MAA is added to ZPO (molar ratio 1:1) and stirred for 15 minutes to form the Zirconium complex. The hydrolyzed MAPTMS is then added to the ZPO-MAA complex in a 2:8 molar ratio and stirred for another 15 minutes. The quencher DMAEMA is then added, (MAPTMS+ZPO):DMAEMA molar ratio 9:1, and stirred for another 10 minutes. Finally, 1% w/w of the photoinitiator BIS is added and stirred for 15 minutes. This composite is then filtered using a 0.22 µm pore sized syringe filter.

The sample preparation is done by adding a drop on a 140 µm glass cover slip and then keeping it in the vacuum oven at 40C for 20 seconds. The heating process leads to the formation of an inorganic matrix, which converts the drop into a gel which enables printing complex 3D structures. The synthesis steps were done by Dr. Sanjoy Mukherjee (former post-doctoral researcher) and Teng Chi, PhD student from Prof. Boudouris' group from the Davidson School of Chemical Engineering.

2.3 Scanning Procedure

For 3D structures the CAD model is first sliced into different layers and converted into Gcode using the slic3r program. The CAD model of the truss bridge structure shown in Fig 2.7 (a) is sliced as shown in Fig 2.7 (b) and a Gcode file for the structure is created. This Gcode has the coordinate instructions for the scanning mirror, the z axis of the stage and the EOM so that the focal spot moves in the resin and turns the beam on and off at the required times. The parameters for slicing are the layer height, extrusion width and the scaling factor which fixes the size of the printed structure. The parameters for the structure in Fig 2.7 are 400nm layer height and 300nm extrusion width. These were fabricated using the sample without the quencher added to it. Fig 2.7 (c) shows the SEM image of the printed structure.

For structures that are very small and are printed with a higher resolution by adding the quencher, the conventional style of slicing explained above leads to the structure being thicker at the edges and not smooth on the top. For such structures like the nano antennas like the diabolo antenna a new type of scanning method called overscanning is deviced.

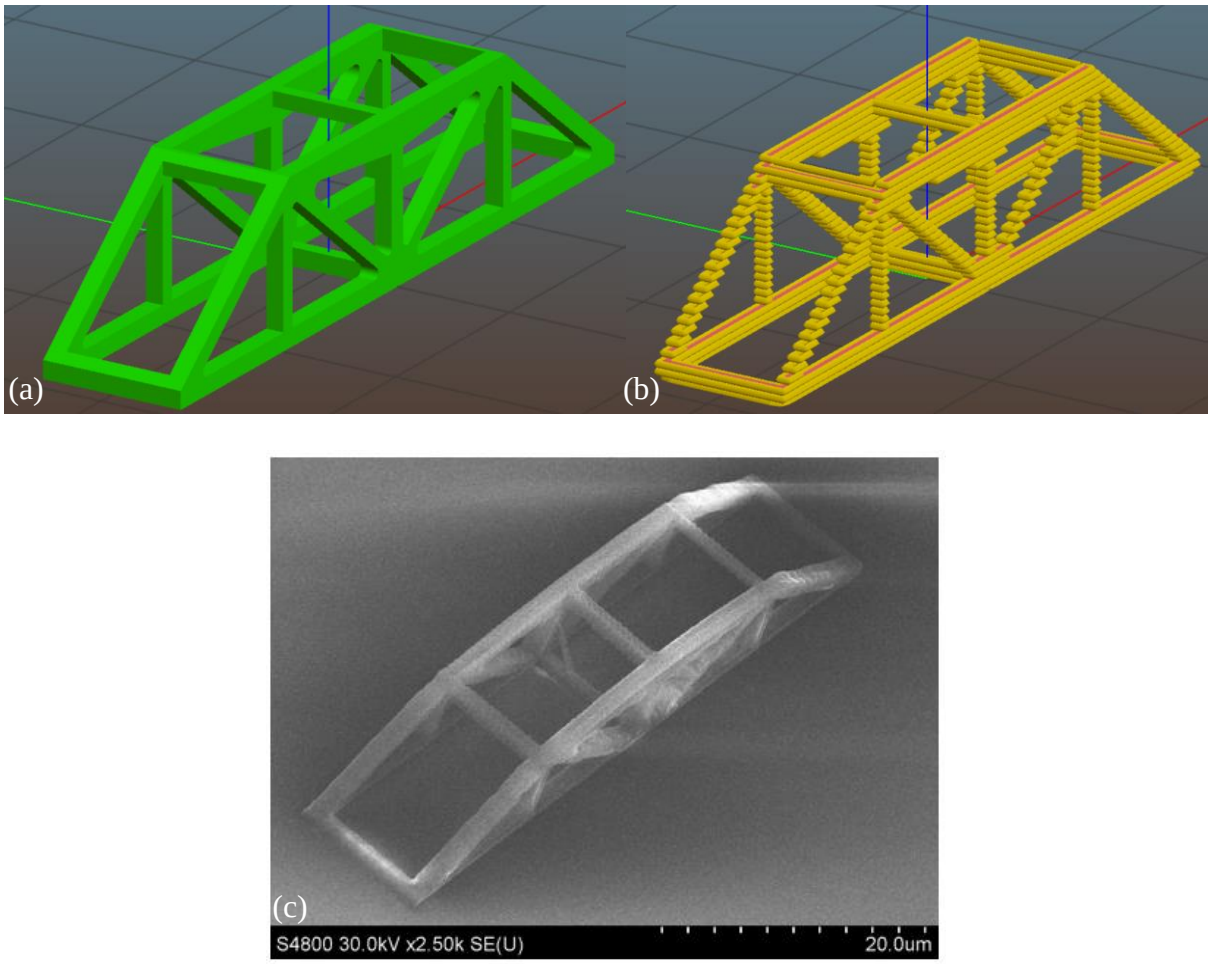

Figure 2.7: (a) CAD model of the truss bridge, (b) slicing, (c) SEM image of printed structure laser power 4mW (measured before objective for all cases), scan speed 200µm/s, 400nm layers.

Overscanning is the scanning pattern shown in Fig 2.8 (d) in which the long lines represent the scan pattern, but the laser is turned on by the EOM only within the triangular pattern, thus creating the triangular structure. This strategy makes a big difference in structure quality of nano antennas. The structure shown in Fig 2.8 (a) is made using the pattern shown in Fig 2.8 (b). The thickening

of the edges is clearly visible, this is due to added dosing of the laser at the edges where the piezomotor of the scanning mirror has to make accelerations and decelerations. In Fig 2.8 (c), the structure is made by overscanning using the same writing speed and laser power. The laser path is shown in Fig 2.8 (d). A higher quality structure is formed with a smooth top which makes printing of the nano antennas possible.

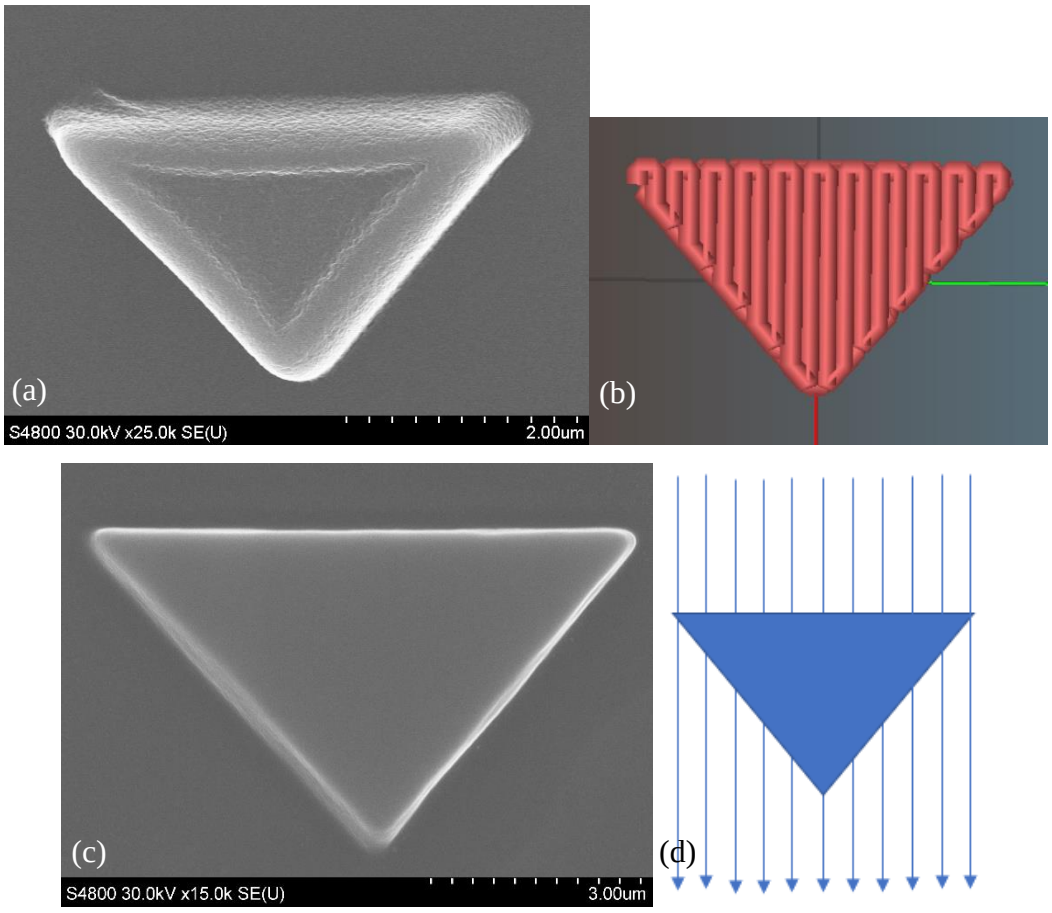

Figure 2.8: (a) SEM image (top view) of a triangle structure formed by conventional scanning, (b) beam path used for (a), (c) SEM image (top view) of a triangular structure formed by overscanning procedure, (d) overscanning pattern – the laser beam is on only inside the triangle, both the structures are made using 20µm/s scan speed, 3.6 mW laser power and 100nm layer height.

The EOM is required in the setup instead of a shutter so that faster turn on/off of the beam is achieved which is instrumental for higher resolution at the edges. The structures are printed using

xy laser scanning by the galvo mirror and z changes by the piezo stage. Moving from one structure to the other, the shift in xy location is done by the xy axes of the piezo stage.

2.4 3D Printed structures

The conventional scanning procedure is used to obtain the initial 3D printed structures printed using the photoresist explained in section 2.2 ((MAPTMS+ZPO):DMAEMA + BIS) without the quencher added. These structures are shown in Figures 2.9 to 2.12

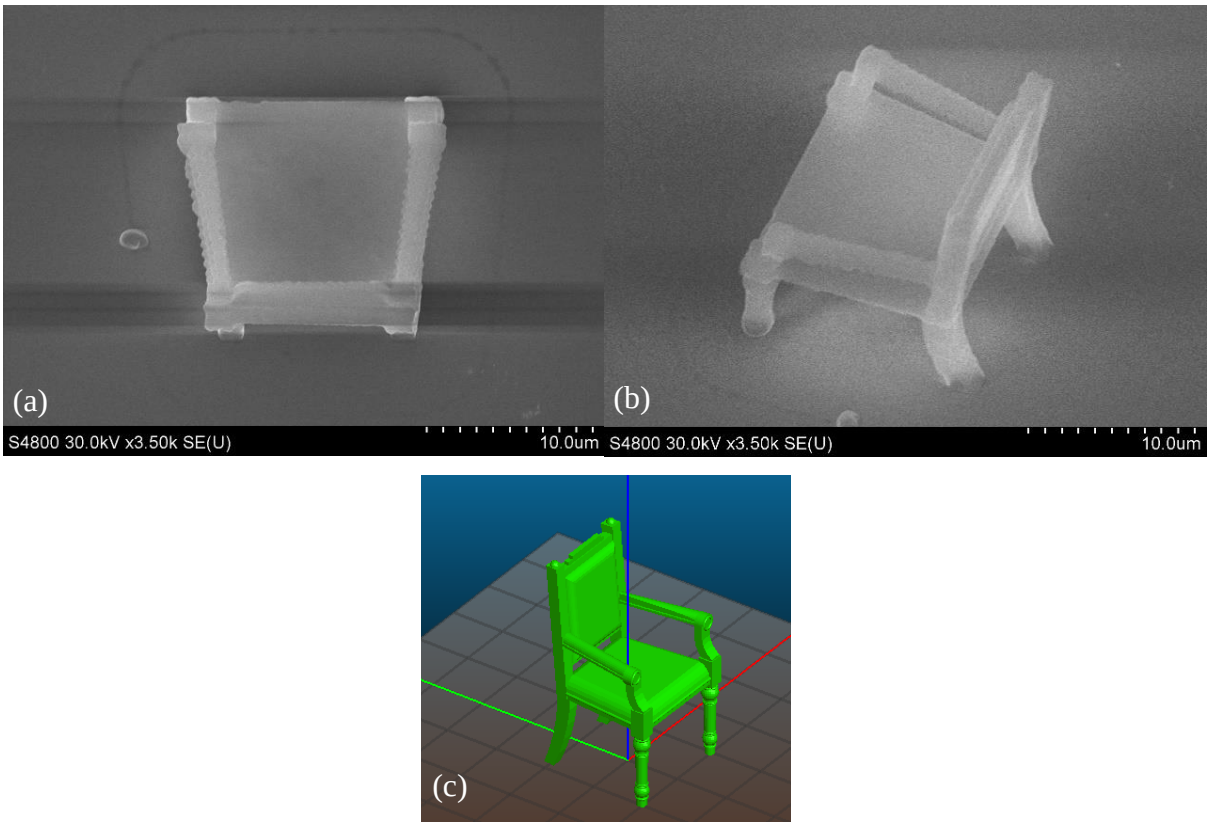

Figure 2.9: (a)Top view and (b) tilted view of printed structure with (c) CAD model, laser power 4 mW, scan speed 200µm/s and 400nm layers for all 3D structures.

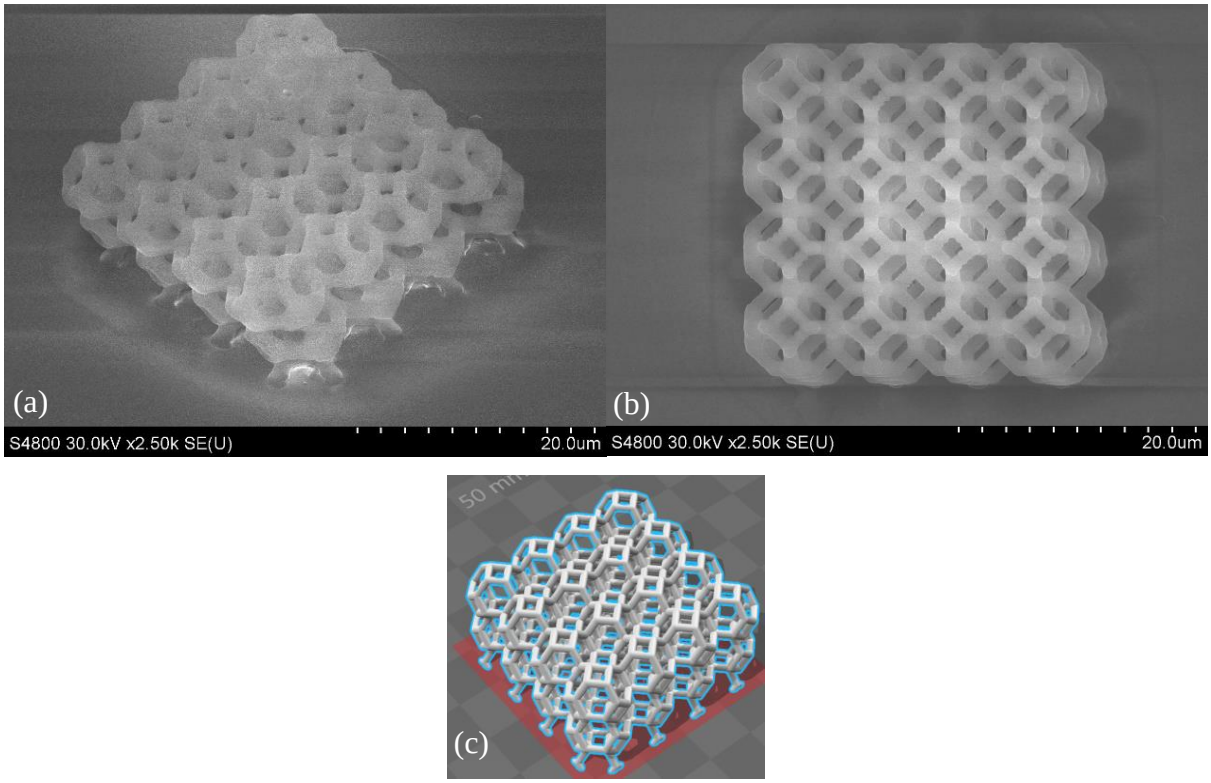

Figure 3.10: (a)Top view and (b) tilted view of printed structure with (c) CAD model.

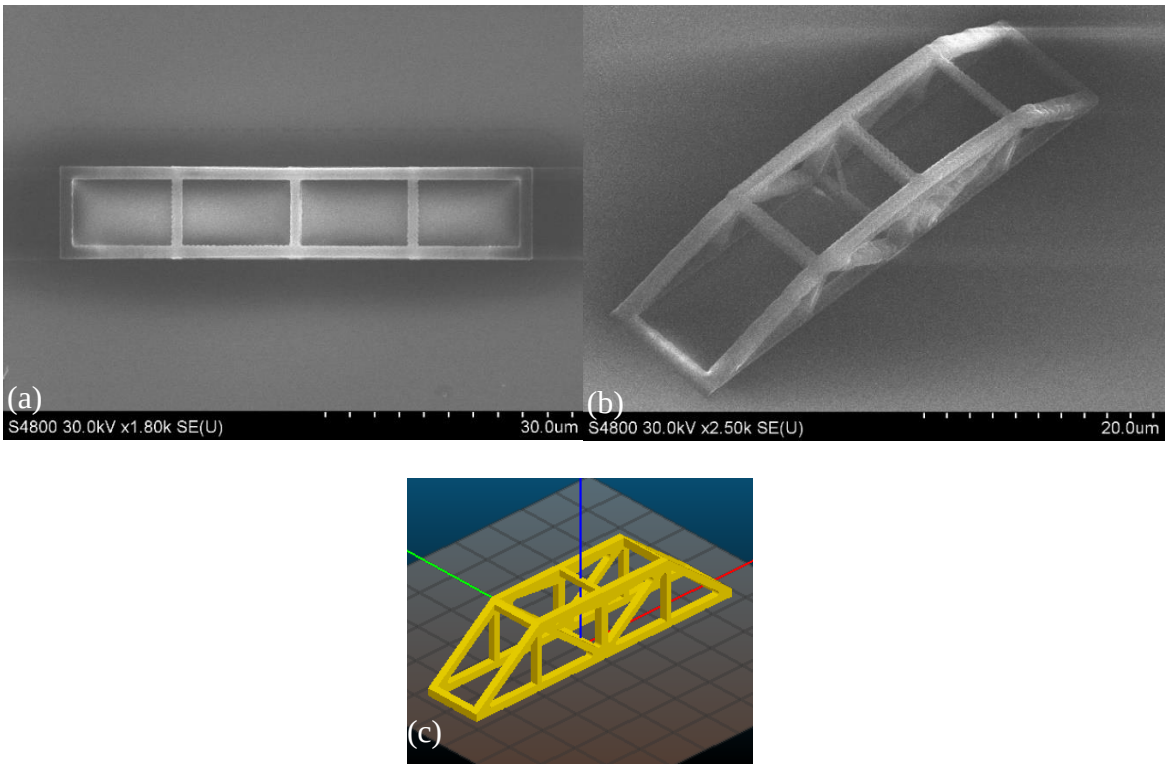

Figure 4.11: (a)Top view and (b) tilted view of printed structure with (c) CAD model.

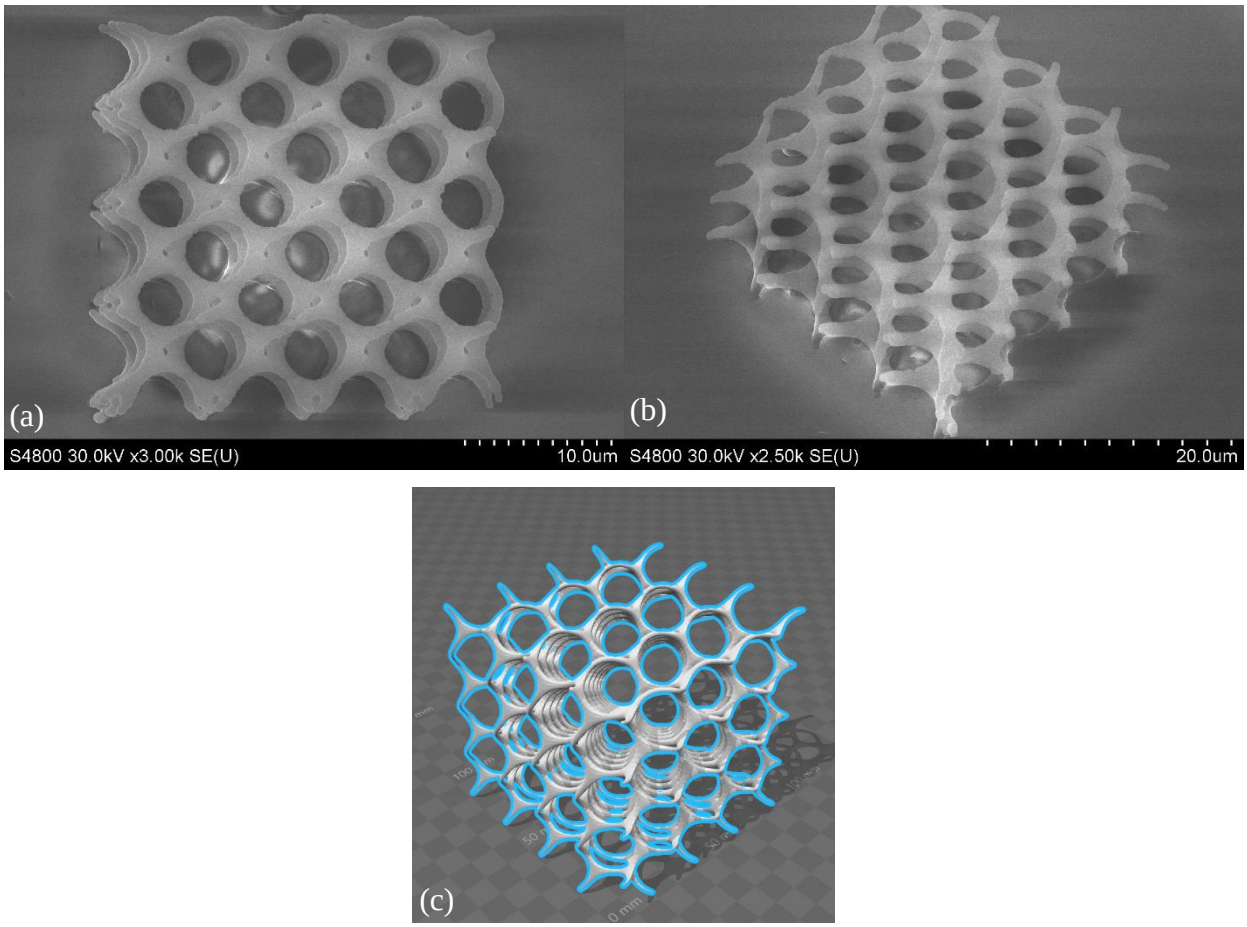

Figure 2.12: (a)Top view and (b) tilted view of printed structure with (c) CAD model laser power 4 mW, scan speed 200µm/s and 400nm layers.

The addition of the quencher (DMAEMA) to the photoresist helps in creating higher resolution structures as the quencher can diffuse through the matrix and cause a depletion of the radicals that are generated [4]. Since the quenching is also dependent on the diffusion, a slower writing speed is required. Fig 2.13 and Fig 2.14 shows a comparison between woodpile structures fabricated with and without the quencher showing a finer feature size with quencher.

Fig 2.14 synthesized using photoresist with the quencher added shows a line width of 120nm and Fig 2.13 synthesized with photoresist without the quencher added shows a feature sizes of 350nm, both of them are fabricated using the same laser power of 2.8mW and scan speed of 20µm/s. This

improved finer feature size enabled the printing of the nanoantenna structures explained in the next chapter.

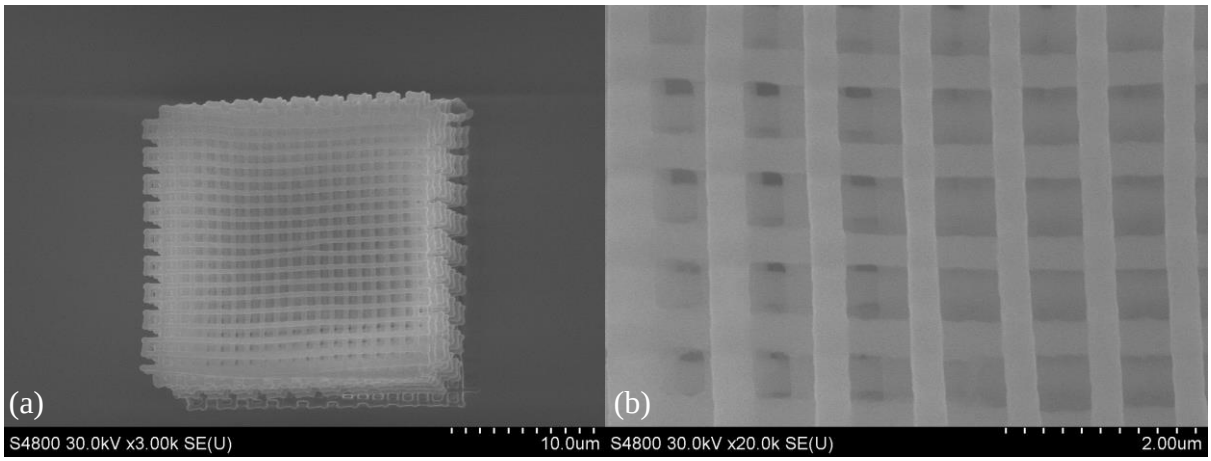

Figure 2.13: Woodpile structure fabricated using photoresist without quencher showing line width of 350 nm, laser power 2.8mW, scan speed 20µm/s.

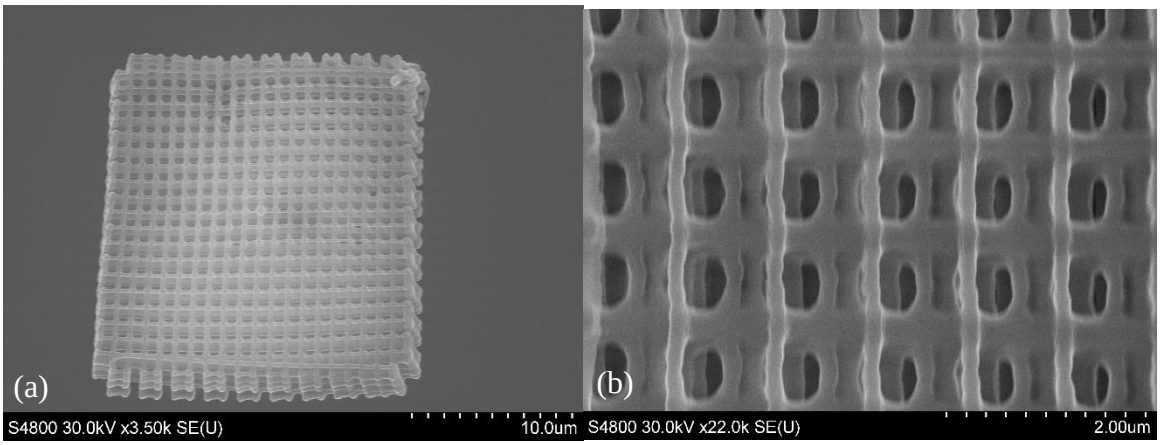

Figure 2.14: Woodpile structure fabricated using photoresist without quencher showing line width of 120 nm, laser power 2.8mW, scan speed 20µm/s.

2.5 Summary

The experiments use the schematic in Fig 2.1 and utilizes the 800nm femtosecond, 80 MHz repetition rate and 30 fs pulse width and an inverted microscope which focuses the beam using a 100x objective with N.A. of 1.49. The beam focal spot is moved in three dimensions by the galvo mirror and the sample movement is controlled by the piezo stage. The mechatronic control is done using LabVIEW programs and FPGA chip. The power is controlled by a variable ND filter in the beam path. The photoresist is synthesized based on the recipe from Sakellari et al [4] with the quencher added for high resolution structures. Figures 2.9 and 2.12 show the 3D structures that were fabricated and Fig 2.13 and Fig 2.14 show a comparison between the feature sizes without and with the quencher added. The overscanning procedure shown in Fig. 2.8 (d) was designed for achieving higher structure quality which is seen in Fig. 2.8 (c). The arrays that are synthesized are coated with 55nm of gold using e-beam evaporation. The process was performed by Prabhu Kumar Venuthurumilli, and Shouyuan Huang, PhD students. The reflectance measurement is done using a Fourier Transform Infrared Spectrometer (FTIR).

3. PRINTING OF NANOANTENNA ARRAY

3.1 Introduction

Metal nanostructures have the ability to create enhanced electromagnetic fields depending on their geometry and pattern. The incident beam generates an electromagnetic near field that is highly localized [12]. The ability of nanostructures to enhance the magnetic field is studied in subwavelength apertures, metal rings, cylinders and split ring resonators [12]. Enhancement of the electric field between closely spaced nanostructures is very well known [12]. Bowtie nanoantenna and bowtie nanoaperture are used for creating such enhanced electric fields [13][14][15] in the gap between the metal structures. The diabolo antenna introduced in 2011 [12] enhances the magnetic field due to the high current density in the metal bridge, between the two triangular sections, which in turn induces this magnetic field as shown in Fig 3.1 (c), explained in detail below.

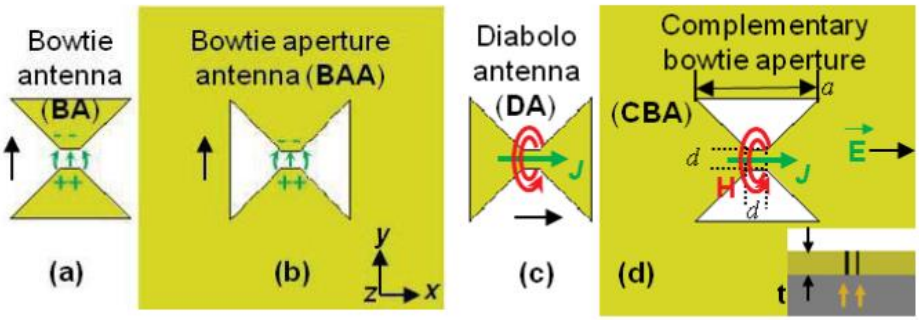

Figure 3.1: Bowtie shaped structures with the correct polarization of excitation shown by the black arrows (a) bowtie antenna - BA, (b) bowtie aperture antenna - BAA, (c) diabolo antenna - DA, (d) complementary bowtie aperture – CBA [16].

As shown in the Fig 3.1 (c), the DA structure consists of two triangular parts made of metal and a bridge that joins them together. This bridge is what distinguishes the diabolo antenna from the bowtie antenna which changes the working principle. In case of the bowtie antenna, the electric

field polarized in the direction shown causes the charge accumulation at the tips as shown in Fig 3.1 (a). This charge accumulation inturn causes an electric field enhancement between the tips because of the capacitive effect. In case of the diabolo antenna, the metal parts act like a funnel which causes the flow of charges through the bridge causing a current through the bridge [12]. This current causes an induced magnetic field according to Ampere's law, which causes a magnetic field hotspot around the bridge.

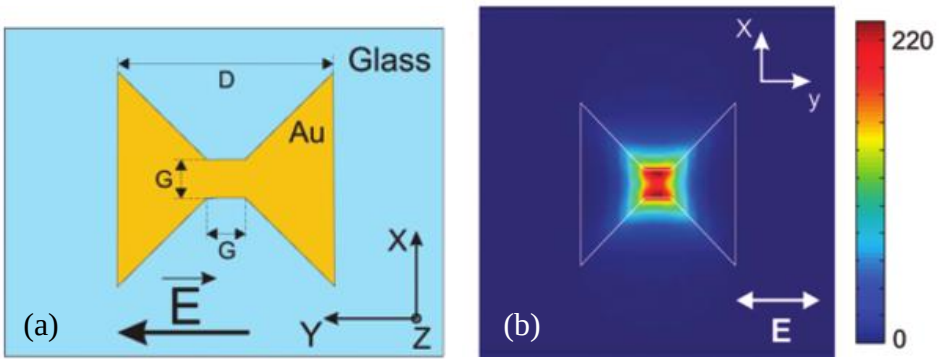

Figure 3.2: (a) simulation model for diabolo antenna showing gold structure of thickness T on glass, other dimensions as shown and electric field polarization direction, (b) Magnetic field enhancement (G = T = 50 nm, D = 310 nm, λ = 1940 nm) excited result showing central hotspot with peak magnetic field enhancement of 220 normalized with the magnetic field without the gold structure [12].

Fig 3.2 (a) shows the simulation scheme for the gold diabolo antenna structure of glass of thickness T, length D and both the length and width of the bridge G. Fig 3.2 (b) shows the simulation result showing the magnetic field enhancement for G = T = 50 nm, D = 310 nm, λ = 1940 nm. The single magnetic hotspot at the center is clearly seen.

This chapter shows 3D printing of diabolo antennas using two photon polymerization. The antennas need to be metallized which is done using a single step of electron beam evaporation. The procedure is explained in the next section.

3.2 Diabolo Antenna Arrays by 3D Printing

The overscanning procedure as explained in section 2.3 is employed in the printing of diabolo antennas. The CAD model of the antenna is first created using Autodesk Inventor and sliced into layers using the slic3r program and converted to Gcode.as explained in section 2.3 This Gcode is used by the LabVIEW program to create the overscanning pattern as shown in Fig 3.3 (d).

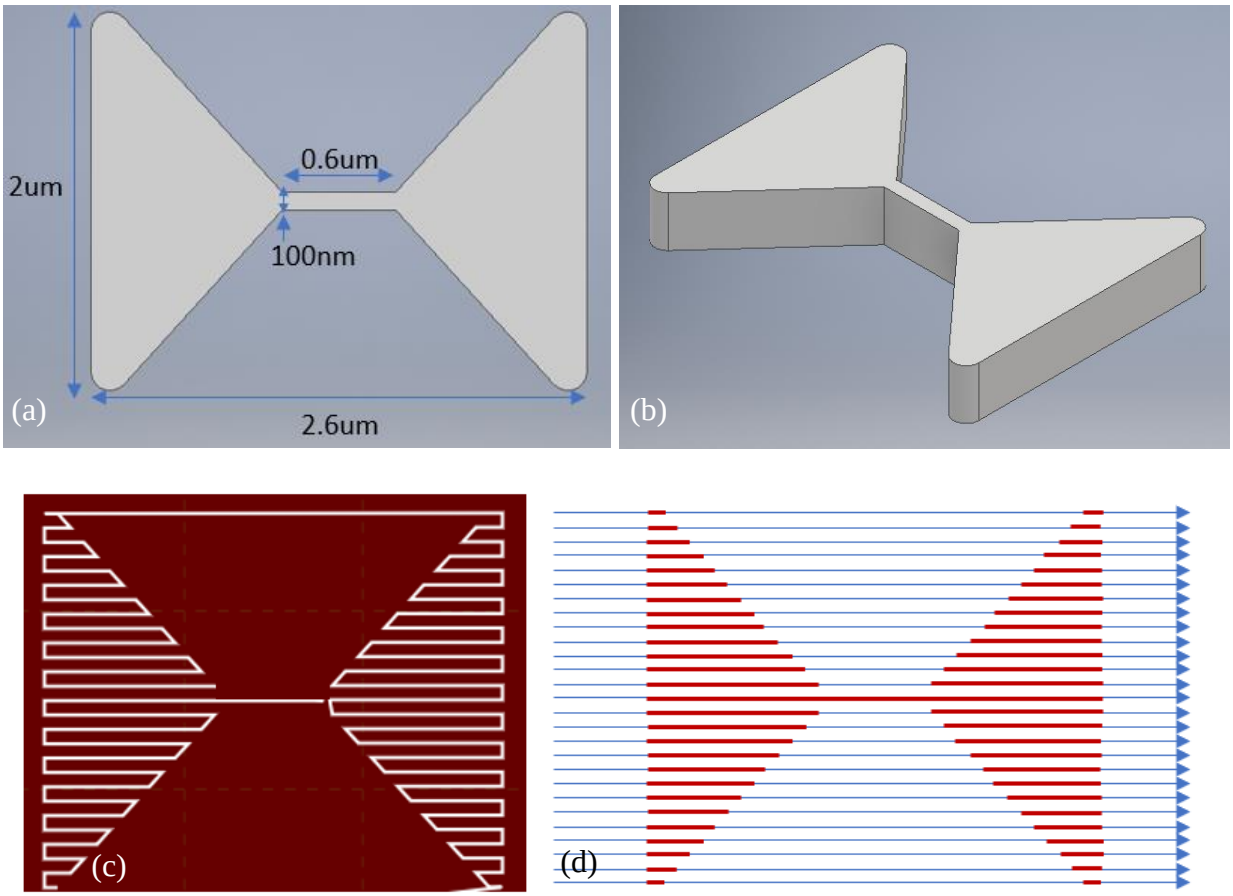

Figure 3.3: (a) The top view of the cad model of the diabolo antenna with dimensions, (b) the tilted view of the antenna with a height of 400nm, (c) the conventional scan pattern for a layer, (d) the over-scan pattern for the layer, the red lines indicate that the laser is on.

The filet radius of 100nm seen at the vertices of the structure are incorporated after experimentally verifying the radius after the printing process. The parameters for printing which includes the laser power, scan speed, layer height are optimized experimentally. It is found that a laser power of

3.8mW, line width of 100nm, scan speed of 40µm/s and a layer height of 100nm gives the best results. Fig 3.7 shows an example of a different writing parameter.

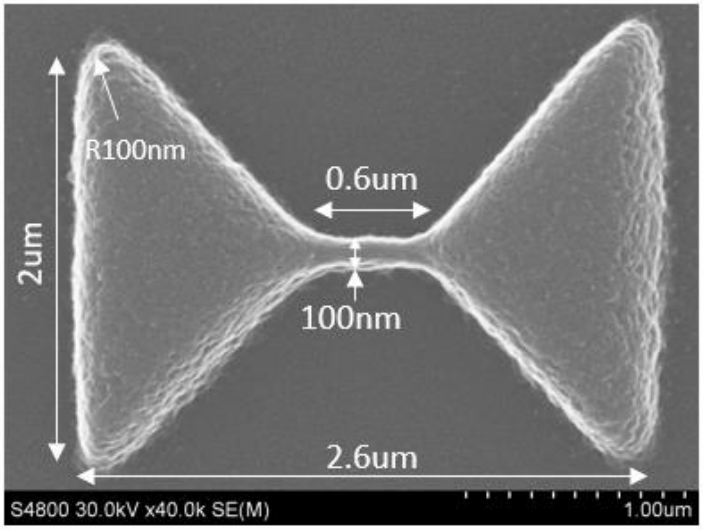

Figure 3.4 SEM image of printed diabolo antenna showing dimensions (top view).

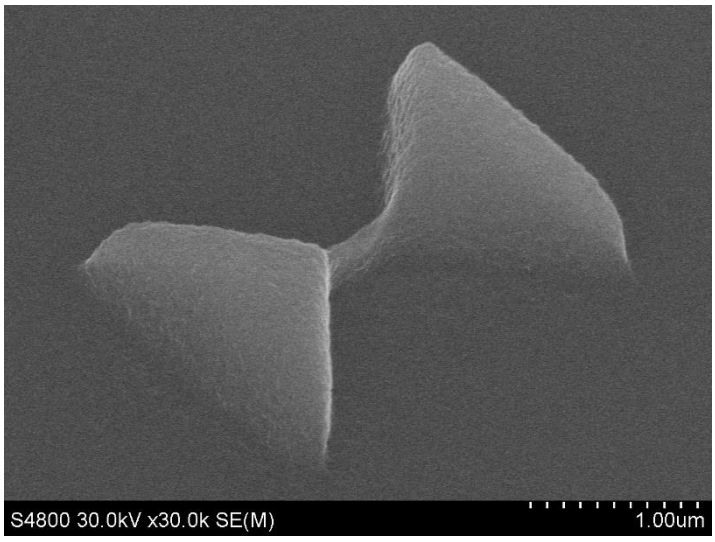

Figure 3.5: SEM image of tilted view of printed diabolo antenna.

Fig 3.4 and Fig 3.5 shows the top view and tilted view of the diabolo antenna structure printed with the optimized parameters. The structure is made of 4 layers of 100nm height making a 400nm tall structure. The tilted view of the diabolo antenna shows that the bridge between the two

triangular structures has a shorter height compared to the triangular part. This will affect the current flow through the bridge after it is coated with gold thereby affecting the magnetic field enhancement that is required. This height difference is due to the fact that the bridge is made up of only 4 layers of a single line scan. This issue is resolved by scanning the bridge twice in each layer. Fig 3.6 (a) and (b) shows the SEM image of the resulting printed structure.

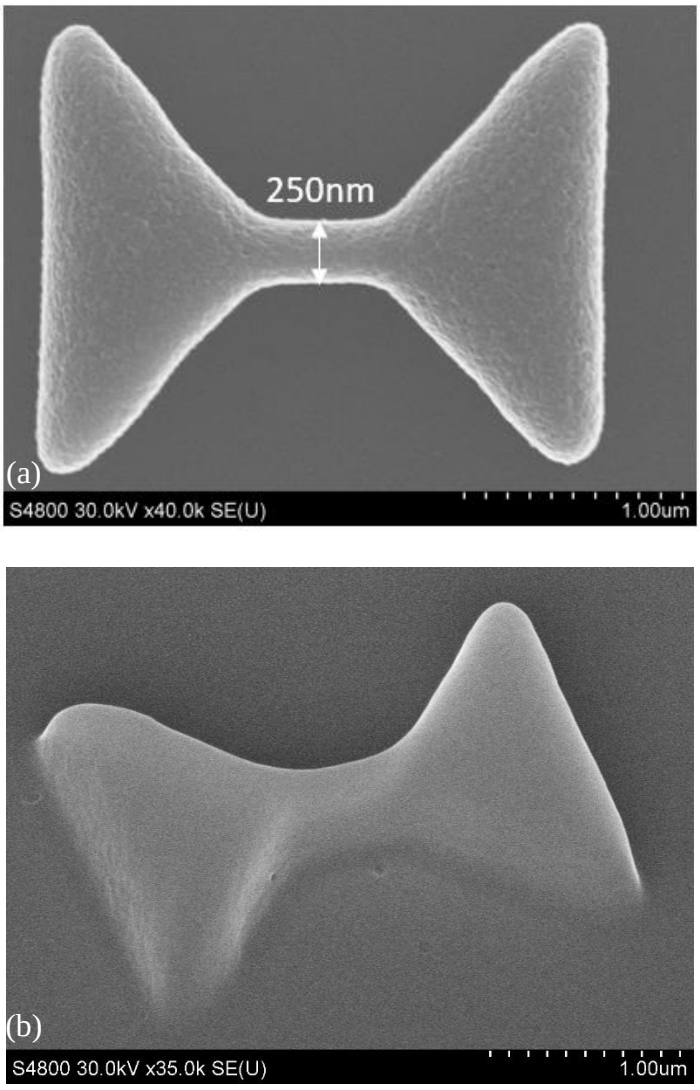

Figure 3.6: (a) Top view and (b) tilted view of diabolo antenna after resolving bridge height issue.

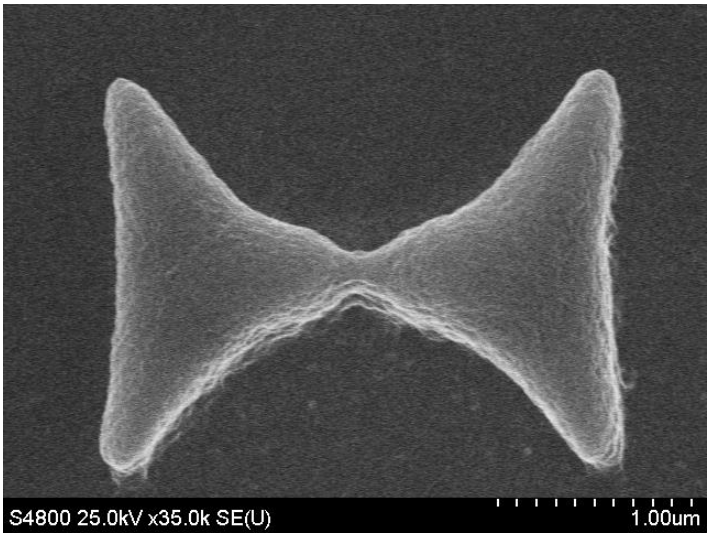

Figure 3.7: diabolo antenna written at different parameters of laser power 3mW, writing speed 10µm/s, 100nm layer height and total height 400nm.

Fixing the bridge height has causes the bridge width to increase to 250nm. This is a compromise that is made so that functional antenna structure can be fabricated. An array of such diabolo antennas need to be made for creating an optical metasurface.

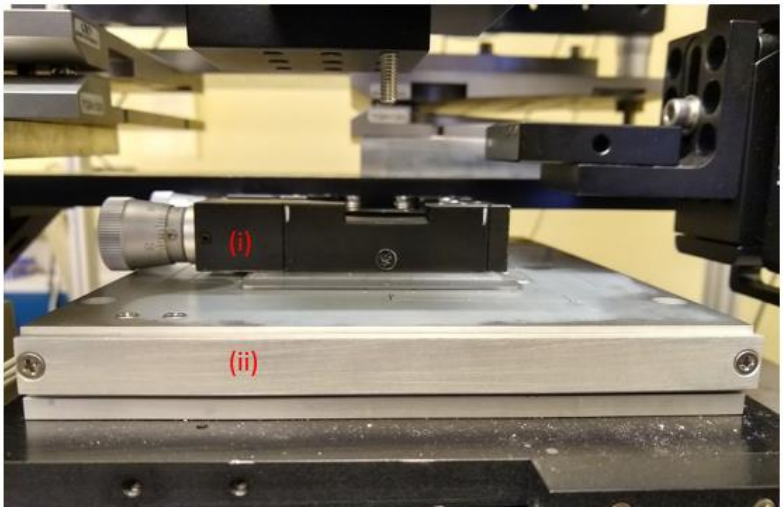

Figure 3.8: The tip-tilt stage (i) mounted on top of the piezo stage(ii), the pitch and roll adjustment knobs are seen on the left side of (i). Sample is mounted on (i).

Printing an array of antennas of 40×40 µm or 50×50 µm on a coverglass substrate requires the repetition of the overscan procedure explained above at all the required antenna coordinates. The

alignment of the substrate with respect to the laser beam forms a critical component of the quality of the array and the repeatability of the antennas. The substrate is aligned with respect to the beam by carefully observing the focal spot image on the CCD at the four corners of a 100µm×100µm square by moving the piezo stage to these corners and adjusting the pitch and the roll of this stage shown in Fig 3.8.

After the alignment process, the piezo stage is moved to each of the required coordinates and focused and diabolo antennas are printed. After moving to each of the locations, slight focus adjustments are done to compensate for slight drifts in focus. An autofocusing system that can be integrated into the writing can be a valuable addition to the system as explained in the section on future work. The printed arrays are coated with gold of 55nm in thickness by e-beam evaporation and the images are shown in Fig 3.9 and Fig 3.10.

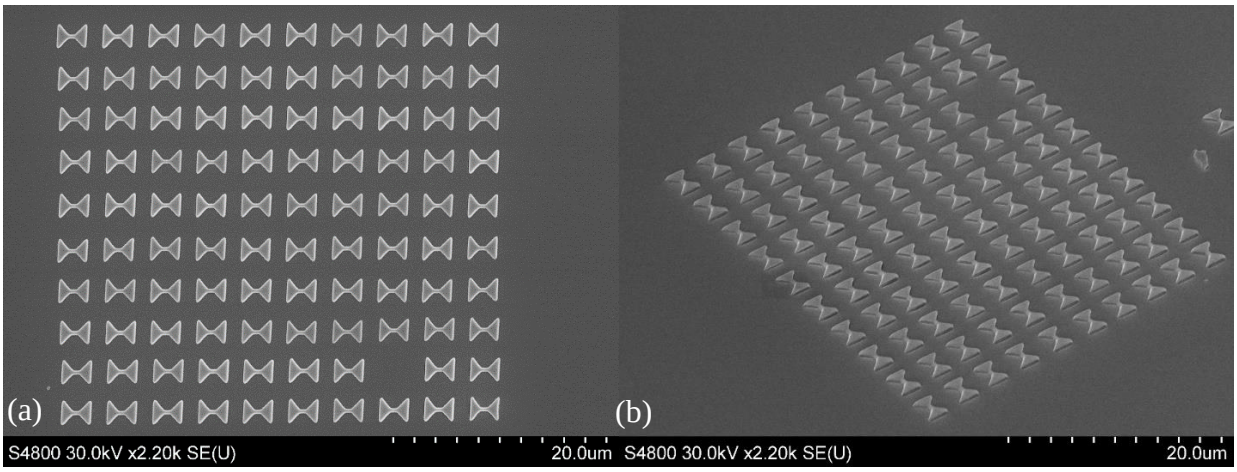

Figure 3.9: (a)top view of a 40µm square array with a 10×10 pattern with periodicity in the x and y direction of 4µm each, the array is coated with 55µm of gold, (b) tilted view of the same structure, writing parameters power – 3.8mW, scan speed - 40µm/s and layer height - 100nm.

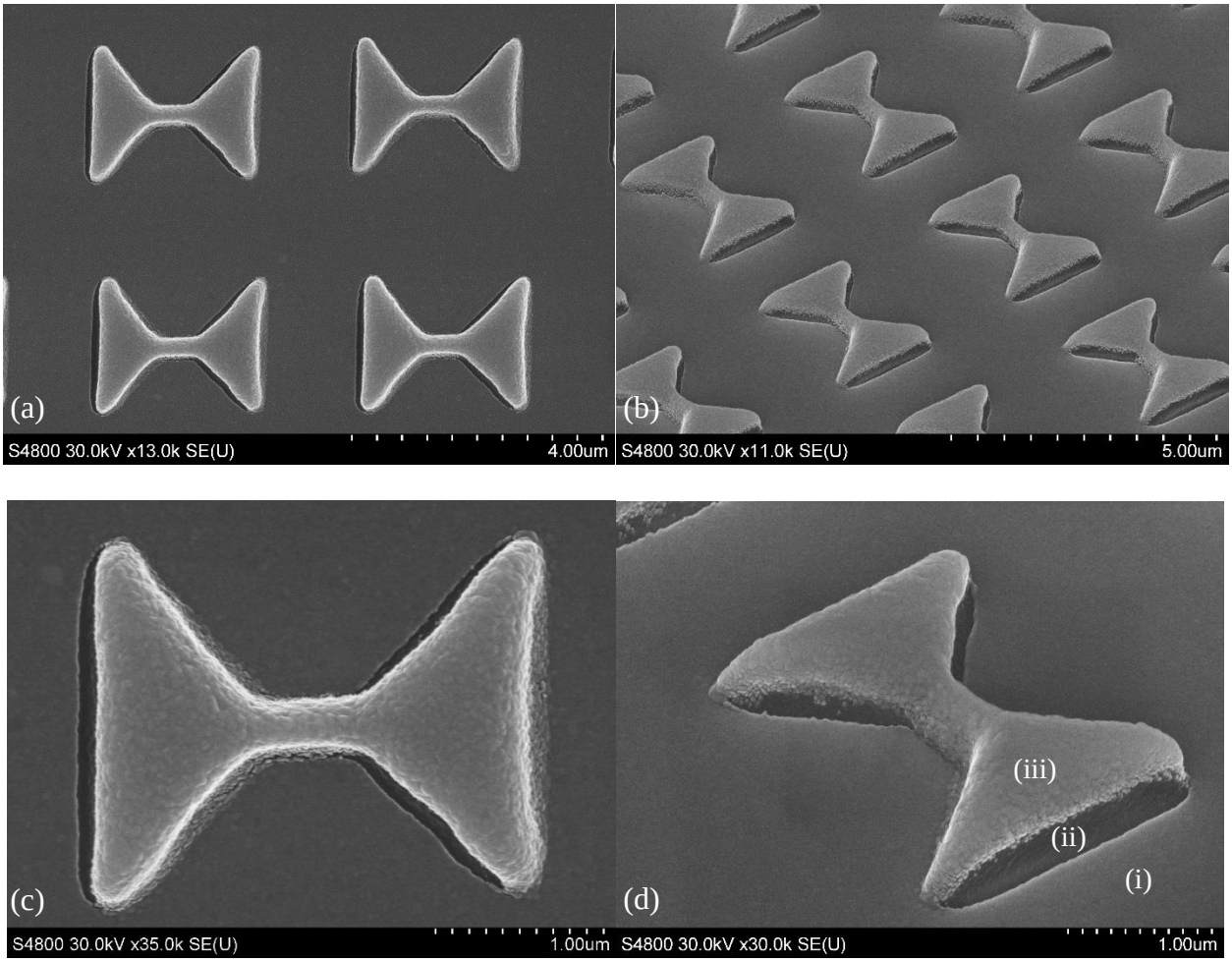

Figure 3.10: (a) close up view of the top view of the array showing 4 antennas, (b) close up view of the tilted array, (c) top view of single antenna, (d) tilted view of single antenna showing layers of the gold layer on glass forming BAA (i), polymer layer (ii) and gold coating on antenna (iii).

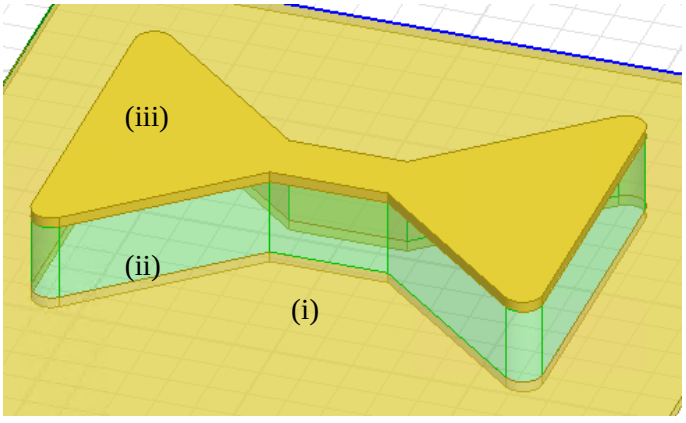

Figure 3.11: the BAA (i), the Diabolo Antenna (DA) (iii) and polymer (ii).

The close up view of the coated antenna clearly shows the gold base layer (i), polymer layer (ii) and gold coating on antenna (iii) in Fig 3.10 (c). It is clearly seen that the gold base layer has an aperture below the polymer layer which is the same as a Bowtie Aperture Antenna (BAA) shown in Fig 3.1 (b). The scheme is shown in Fig 3.11. The polymer is sandwiched by the BAA at the bottom and the DA at the top.

3.3 Simulation of optical response of the nanostructure array

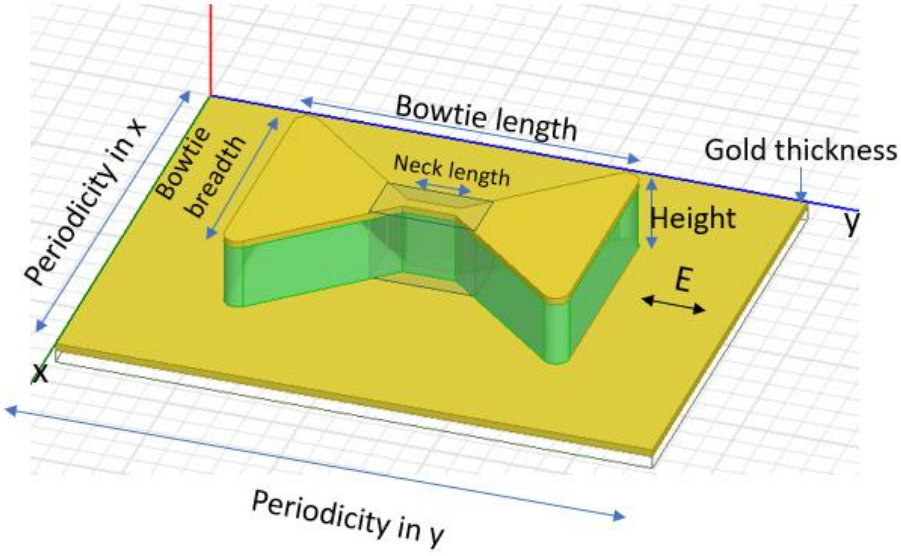

Figure 3.12: The geometry for simulation showing the various parameters that are involved

The nanoantenna array is simulated using ANSYS HFSS. The simulation is setup as shown in Fig 3.12 showing the parameters involved. For the simulation model, there is the gold base layer (BAA), the antenna structure made of polymer, and then the gold coating above the antenna (DA). There is no gold below the polymer. Plane wave of light of 1W power, polarized in the direction shown in the figure is incident on top of the structure and the electromagnetic fields, reflection, absorption and transmission are calculated by the software using a finite element solver.

A periodic boundary condition is followed in the simulation. The parameters that are varied to optimize the structure are height of the structure, the periodicity in x, periodicity in y, bowtie length, bowtie breadth, neck length, neck width and the thickness of the gold coating as can be seen in Fig 3.12. The array shows a dip in reflectance and the parameters are optimized so that the dip reaches zero and there is no reflection of a particular wavelength. The reflectance plot for the optimized array is shown in Fig 3.13 and shows a reflectance drop to zero at 4.04 µm. The parameters for the

optimized array are: height of the structure , h = 400nm, periodicity in x = 4 µm, periodicity in y = 4 µm, bowtie length, bl = 2.6 µm, bowtie breadth, bw = 2 µm, neck length, nl = 600 nm, neck width, nw = 250 nm, thickness of gold coating, t = 55 nm. Figures 3.14 to 3.19 show the plots for varying the parameters involved to find the optimum values. The objective is to have zero reflection for a wavelength of 4.04 µm.

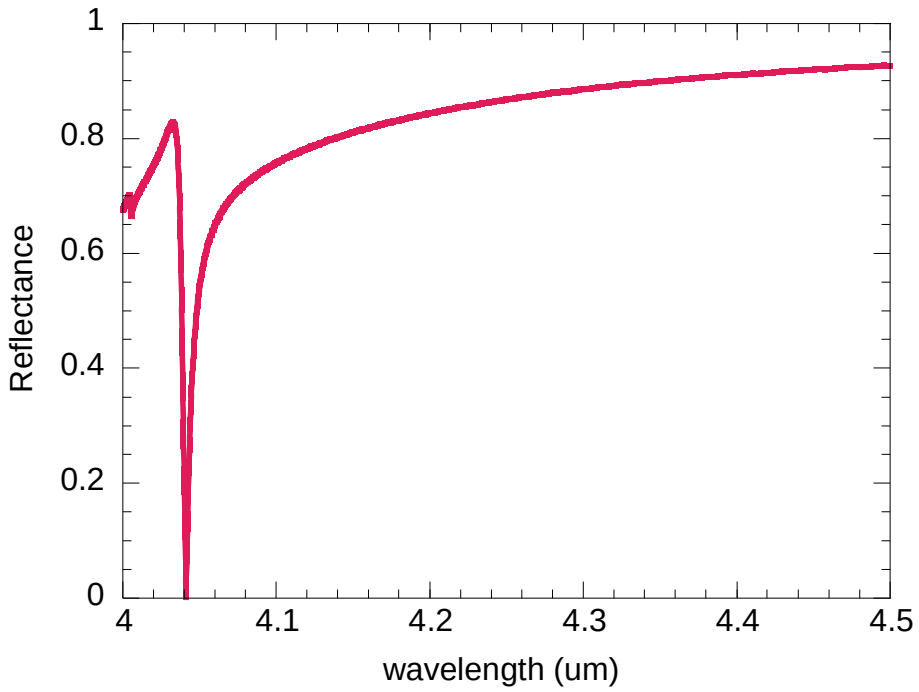

Figure 3.13: Reflectance plot for optimized structure showing reflectance dip at 4.04 µm.

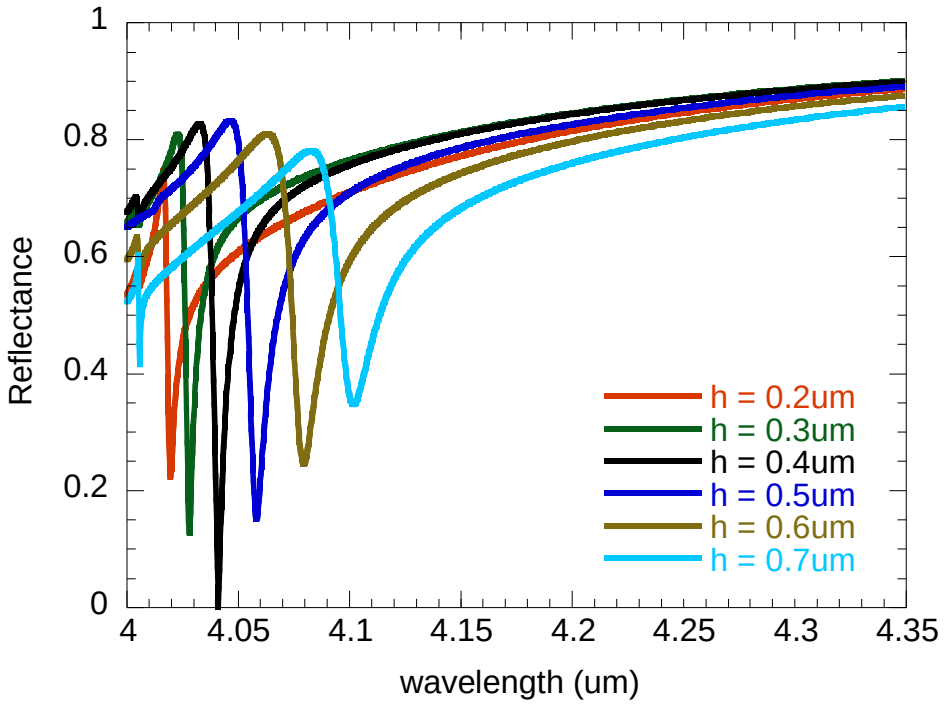

Figure 3.14: varying the height (h) of the antenna showing reflectance drop to zero for 0.4 µm height.

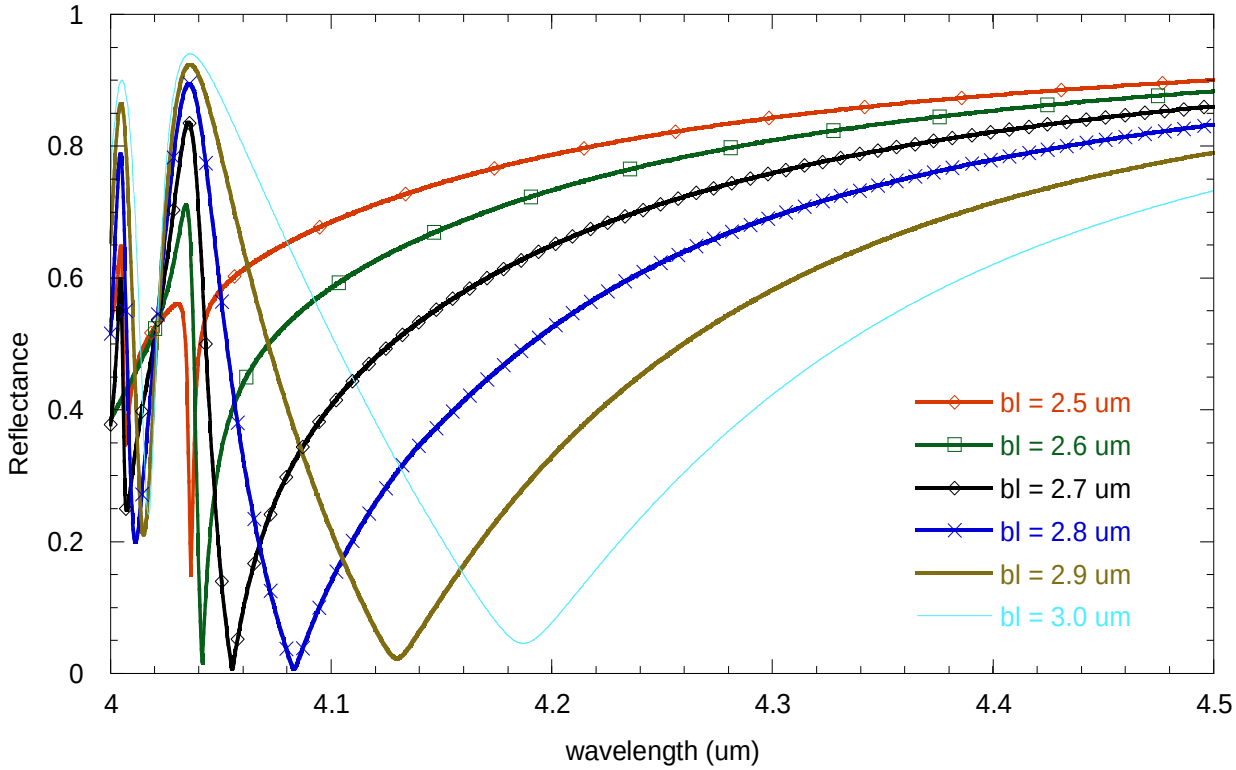

Figure 3.15: varying length of bowtie (bl) showing zero reflection for bl = 2.6 µm.

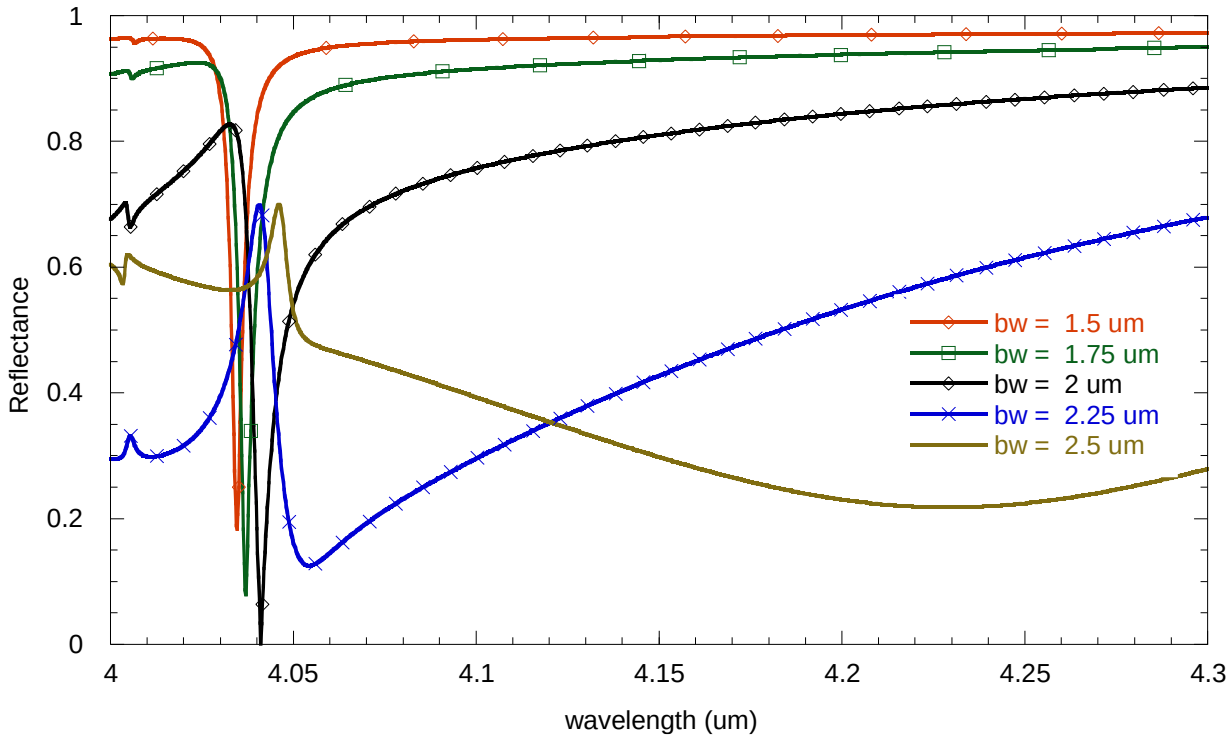

Figure 3.16: varying bowtie width (bw) showing zero reflection for bw = 2µm.

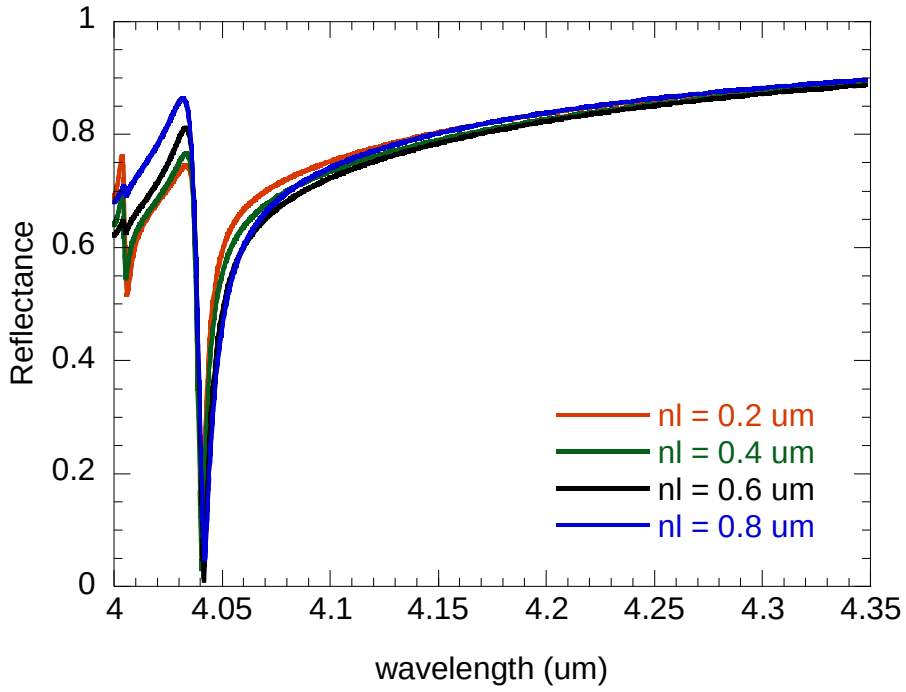

Figure 3.17: varying neck length (nl) shows that it does not have a large impact and chose optimum nl = 0.6 µm.

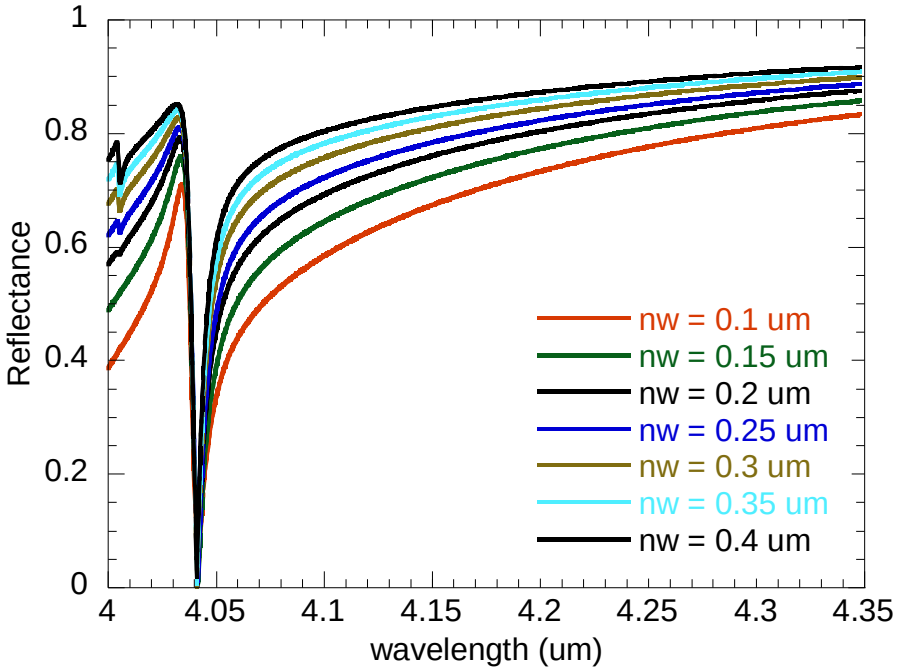

Figure 3.18: varying neck width (nw) shows that it does not have a large impact and chose optimum nw = 0.3µm.

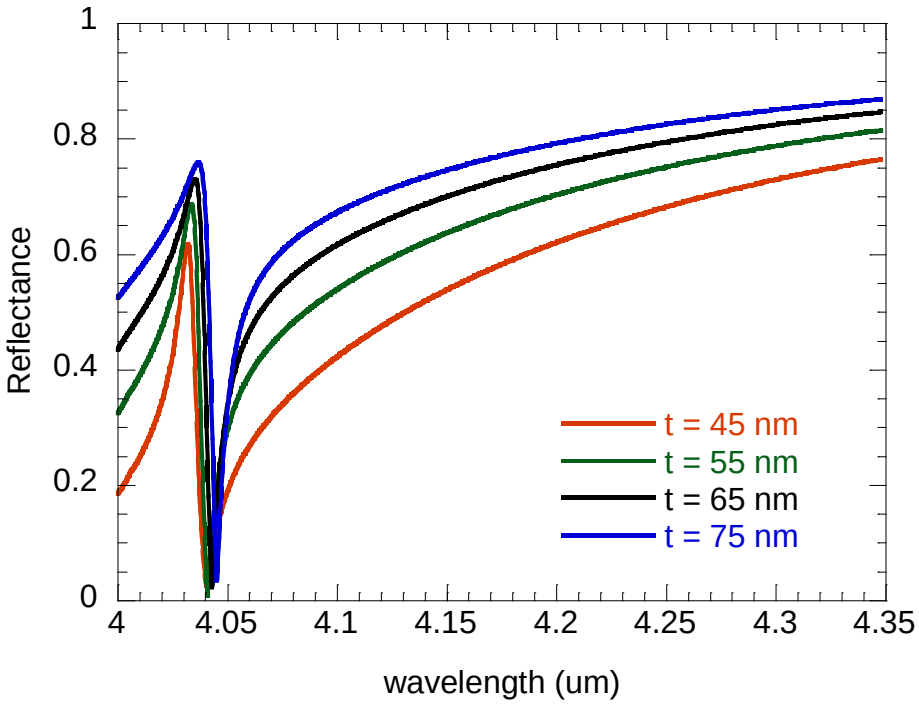

Figure 3.19: varying gold thickness (t) shows that it does not have a large impact and optimum t is chosen as 55nm.

Figures 3.14 to 3.19 show the variation of parameters to find the optimum values. The figures are plotted by varying one parameter while keeping the other parameters constant. From the figures it is clear that the parameters of height, bowtie breadth and bowtie length have more effect on the reflection properties compared to neck length, neck width and gold thickness. To study the cause of the effect at this particular wavelength, the electric field, magnetic field and current is plotted at both the resonance condition and off resonance in figures below.

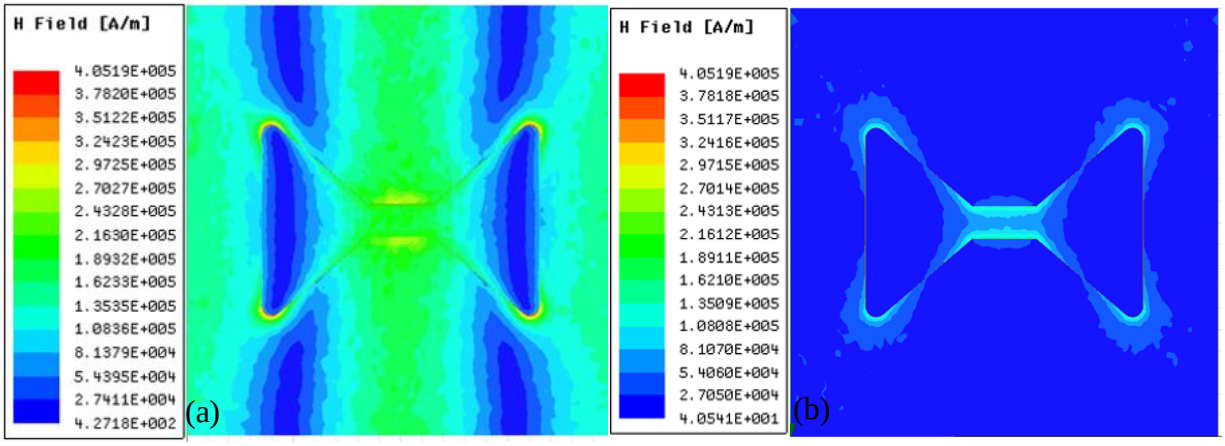

Figure 3.20: (a) magnetic field on antenna and aperture at resonance condition of 4.04 µm, (b) magnetic field on antenna and aperture at off resonance condition of 4.35 µm.

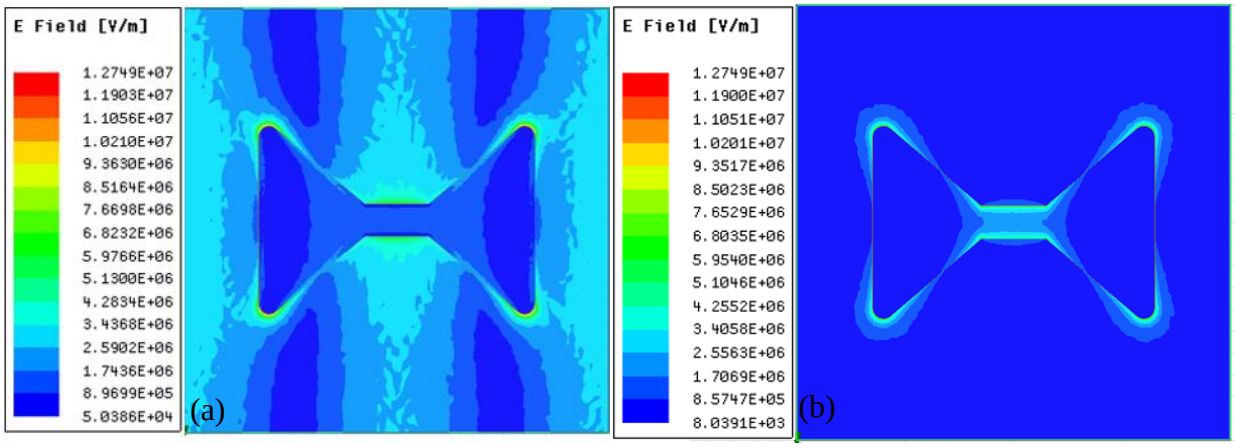

Figure 3.21: (a) magnetic field on antenna and aperture at resonance condition of 4.04 µm, (b) magnetic field on antenna and aperture at off resonance condition of 4.35 µm.

Fig 3.20 and Fig 3.21 show that both the electric field and the magnetic field enhances at the resonance condition. At resonance as expected there is the flow of current through the bridge/neck of the diabolo antenna as shown in Fig 3.22 (b), there is a higher current flow at the aperture plane.

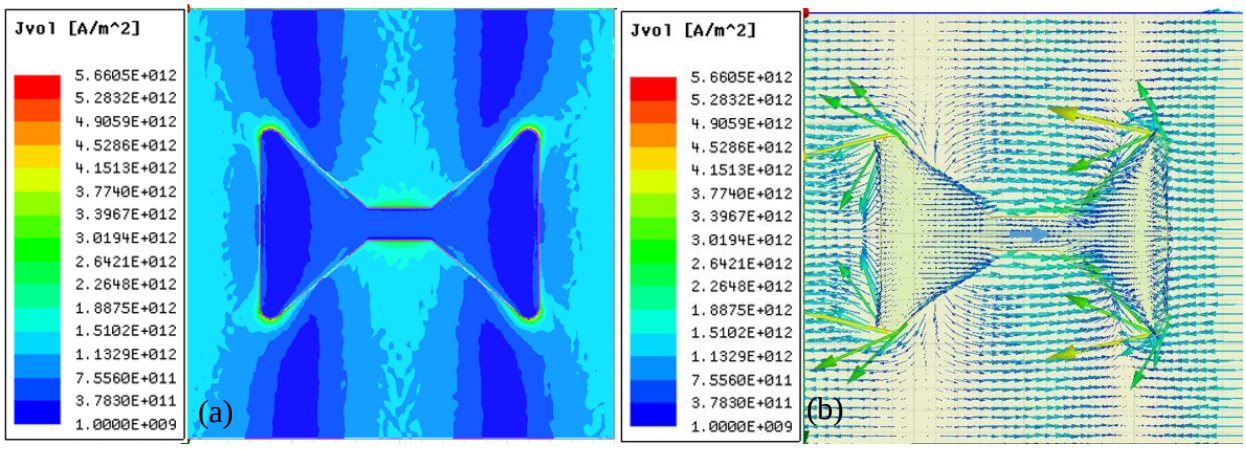

Figure 3.22: (a) current density plot at resonance (b) current density vector plot at resonance.

Field plots on the sectional plane shown in Fig 3.23 gives an insight into the interaction between the antenna and the aperture. Electric and magnetic fields are plotted on this plane at resonance and off-resonance condition.

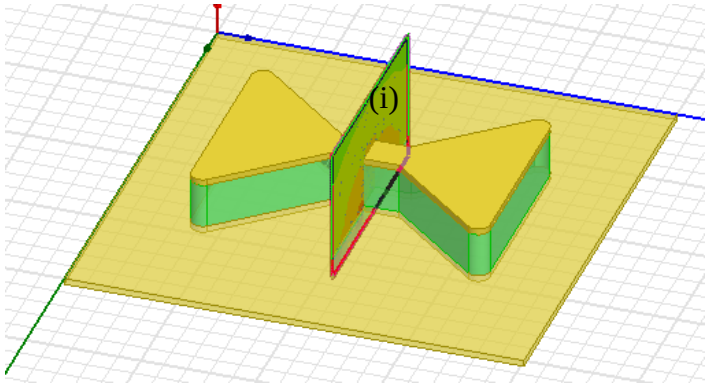

Figure 3.23: the cross-sectional plane (i) at the center of the antenna used to plot the fields.

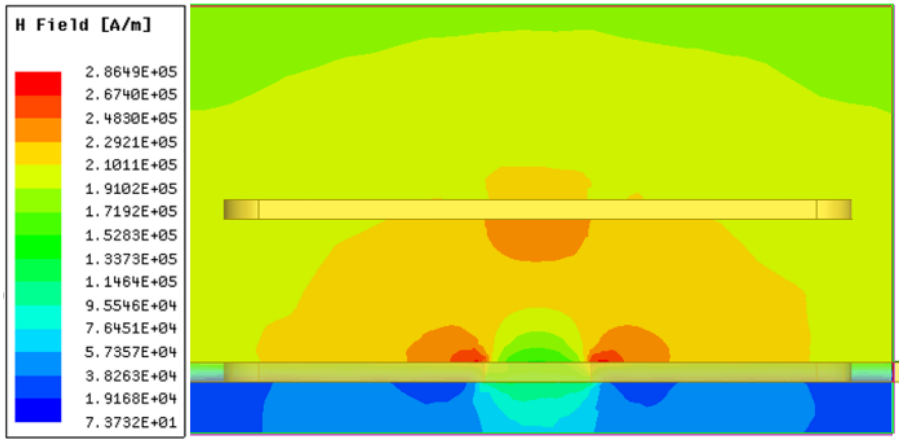

Figure 3.24: Magnetic field at resonance - the magnetic field hotspots between the aperture and the antenna happens only at resonance condition.

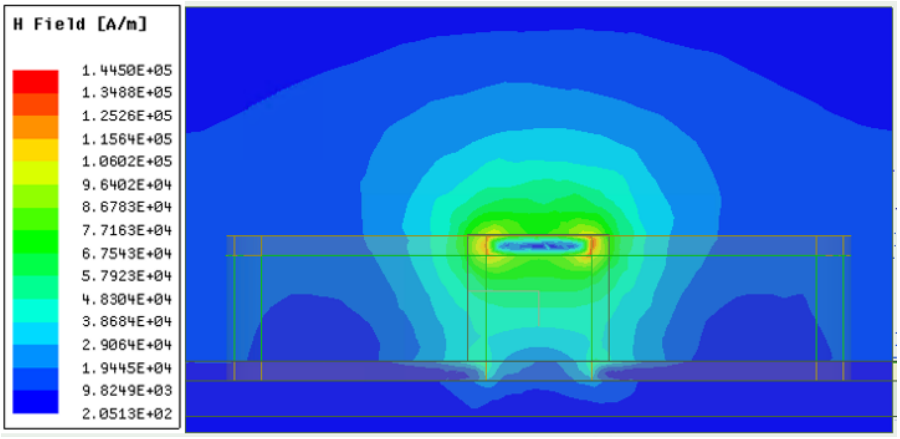

Figure 3.25: magnetic field off resonance.

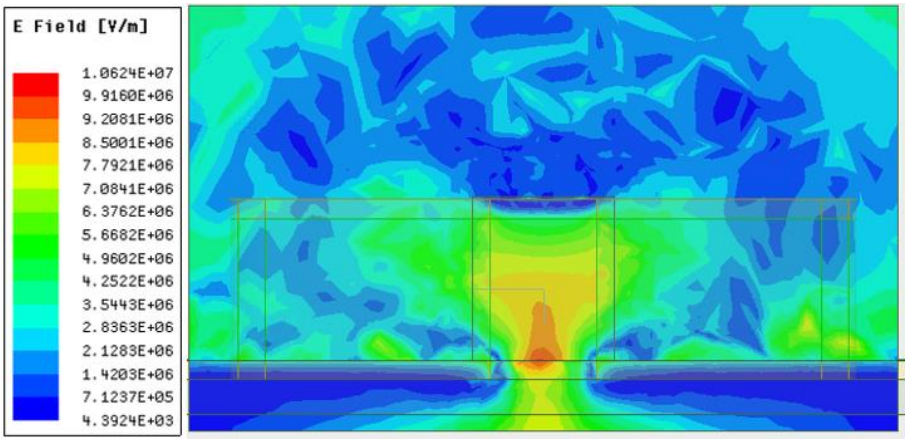

Figure 3.26: Electric field hot spot at resonance.

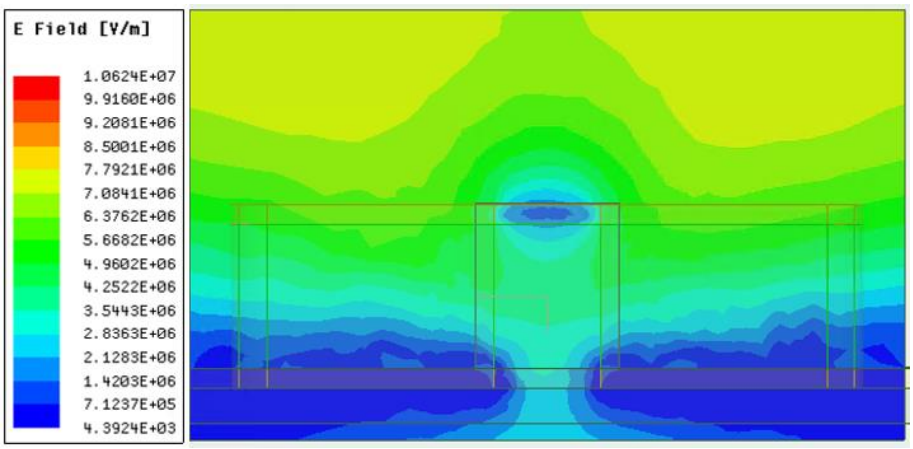

Figure 3.27: Electric field off resonance.

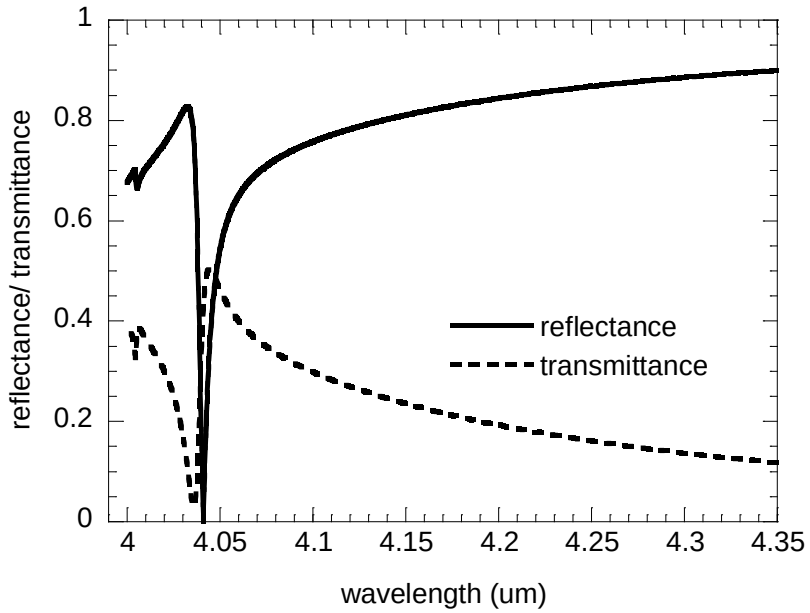

Figure 3.28: reflectance and transmittance for optimum structure.

Fig 3.24 shows an area of high magnetic field and hot spots between the aperture and the antenna. This happens only at the resonant wavelength and only when the dimensions of the bowtie and the array are the optimum dimensions that are calculated. For example, when the height between the aperture and antenna are not the optimum height the hotspots do not occur, and the plot resembles Fig 3.25. The electric field hot spot can also be seen at the resonance condition in Fig 3.26. It is

also observed that the electric field crosses over to the other side of the aperture seen at the bottom part of the figure. This justifies the fact that there is also a transmittance peak very close to the reflectance dip as can be seen in Fig 3.28. For calculation of the energy absorbed by the antenna and the aperture, the dissipated power density (volumetric loss density) shown in Equation (3.1) can be calculated and integrated over the structures.

$$q = \frac{1}{2}\epsilon_0 \omega \, Im(\epsilon)|E|^2 \tag{3.1}$$

where ε is the relative permittivity, ε_0 is the vacuum permittivity, and ω is the angular frequency [16]. The integrated absorption in the antenna and polymer is negligible and that in the aperture is shown in Fig 3.29.

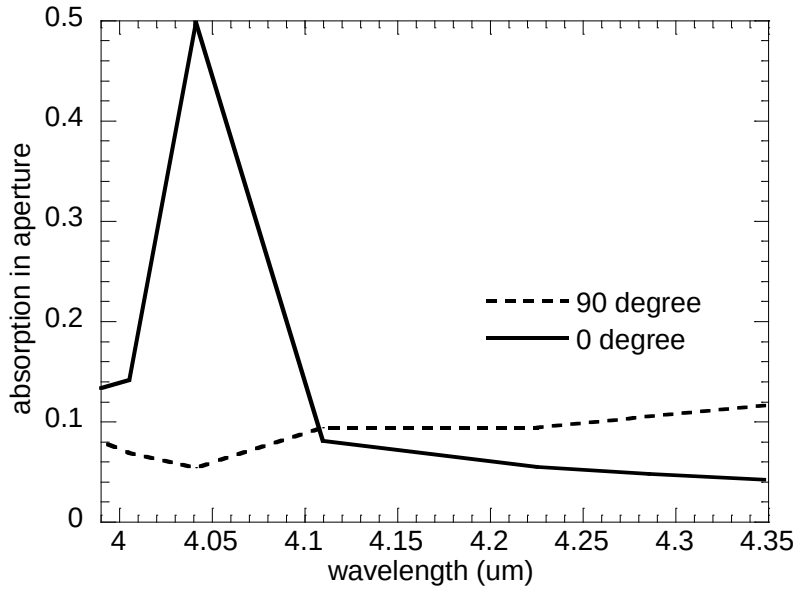

Figure 3.29: Calculated absorption in aperture for the incident wave polarization direction shown in fig 3.12 represented as 0 degree and the polarization direction perpendicular to it shown as 90 degree.

The absorption in the aperture reaches a peak of 0.5 at the resonant wavelength for light polarized along the antenna direction as seen in Fig 3.29 and the transmittance value at resonance from Fig 3.28 is 0.5. Since the reflectance at resonance is zero, approximately 50% light gets absorbed and

50% gets transmitted. Further detailed study into the mechanism of how antenna and aperture work together is a scope of future work.

3.4 FTIR Reflectance Measurement

Fourier Transform Infrared Spectrometer (FTIR) reflectance result for the antenna array shown in Fig 3.9 is shown in Fig 3.30. The plot shows a polarization dependent reflectance dip to 40%, but at a wavelength of 6.6 µm compared to 4.04µm that was predicted in simulation. This might be due to errors in fabrication like small variations in the dimensions and locations of antenna with respect to each other. As predicted the dip is not present at perpendicular polarization. Vasudevan Iyer and Hakan Salihoglu PhD students helped with the setting up, troubleshooting and use of the FTIR system.

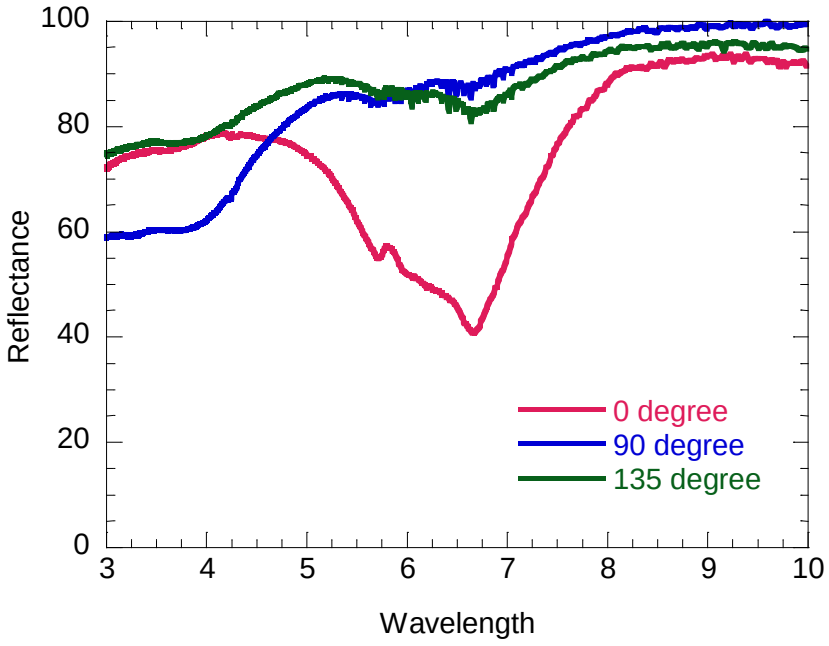

Figure 3.30: FTIR reflectance measurement for incident light polarized along the antenna (0), perpendicular to antenna (90) and at an angle of 135 degrees.

3.5 Summary

Metal nanostructures have the ability to create enhanced electromagnetic fields depending on their geometry and pattern. Bowtie nanoantenna, bowtie nanoaperture are used for creating such enhanced electric fields in the gap between the metal structures. The diabolo antenna introduced in 2011 enhances the magnetic field due to the high current density in the metal bridge between the two triangular sections. Diabolo antenna is printed using the over-scan procedure and an array of the antennas is printed by moving to each antenna coordinate by the piezo stage. Simulation of the structure is done using ANSYS HFSS. The diabolo antenna, polymer, bowtie aperture antenna system is used, and plane wave polarized along the direction of the antenna is incident on this system. A periodic boundary condition is used. The antenna parameters are optimized by simulations and effects of variation of critical parameters are shown in the plots and a zero reflection at resonance condition of 4.04 μm is found. Absorbance is calculated using the volumetric loss density equation. The absorption in the antenna and polymer is negligible and absorption in the aperture peaks at 50% at the resonance condition. Transmittance plot shows that there is a transmittance peak close to the reflectance dip at resonance and ~50% of the light gets transmitted at resonance. FTIR experiments show a polarization dependence dip to 40% at a wavelength of 6.6 μm. This change in location of the dip and a shallower dip might be due to errors in fabrication like small variations in the dimensions and locations of antenna with respect to each other. Further detailed study into the mechanism of how antenna and aperture work together and how fabrication can be optimized further is a future work direction.

4. CONCLUSIONS AND FUTURE WORK

4.1 Summary and Conclusions

In this work two photon polymerization is explored as a method for 3D printing an array of diabolo antenna structures and study the properties. The fabricated antenna structures are coated with gold using an e-beam evaporator to metallize the structure and the optical metasurface is analyzed using an FTIR to measure its reflectance properties.

Part of experimental setup and the programs to control had to be implemented and optimized for this work. The setup mainly involves the femtosecond laser, EOM, variable ND filter, tip/tilt scan mirror and a piezo stage on which the sample is mounted. The EOM controls the turning on and off of the laser, the variable ND filter is used to set the power , the tip/tilt scan mirror is used to scan the laser beam in the xy direction, and the piezo stage is used to move the sample in the x, y and z directions. The photoresist was synthesized based on the recipe from Sakellari et al [4]. The ingredients are zirconium propoxide (ZPO), methacryloxypropyl trimethoxysilane (MAPTMS), 2-(dimethylamino)ethyl methacrylate (DMAEMA) is the quencher, methacrylic acid (MAA), Michler's ketone, 4,4-bis(diethylamino) benzophenone (BIS) is the photoinitiator. For 3D structures the CAD model is first sliced into different layers and converted into Gcode using the slic3r program. This Gcode is fed to the LabVIEW program and it has the coordinate instructions for the scanning mirror, the z axis of the stage and the EOM so that the focal spot moves in the resin and turns the beam on and off at the required times. For structures that are very small and are printed with a higher resolution by adding the quencher, the conventional style of slicing leads to the structure being thicker at the edges and not smooth on the top. For such structures like the nano antennas a new type of scanning method called overscanning is implemented.

Initial results are the 3D printing of CAD models of some structures without the addition of the quencher molecule. It was found that with the addition of quencher the smallest feature size can be improved to around 100nm. With this improved resolution and utilizing overscanning procedure, diabolo antenna arrays are fabricated. Simulation of the structure is done using ANSYS HFSS. The diabolo antenna, polymer, bowtie aperture antenna system is used, and plane wave polarized along the direction of the antenna is incident on this system. A periodic boundary condition is used. The antenna parameters are optimized by simulations and effects of variation of critical parameters are shown in the plots and a zero reflection at resonance condition of 4.04 μm is calculated. Absorbance is calculated using the volumetric loss density equation. The absorption in the antenna and polymer is negligible and absorption in the aperture peaks at 50% at the resonance condition. Transmittance plot shows that there is a transmittance peak close to the reflectance dip at resonance and ~50% of the light gets transmitted at resonance. FTIR experiments show a polarization dependence dip to 40% at a wavelength of 6.6 μm. This change in location of the dip and shallower dip might be due to errors in fabrication like small variations in the dimensions and locations of antenna with respect to each other.

The fabrication method discussed in this work which includes two photon printing and e-beam evaporation is found as a viable way for printing nanoantennas. More complicated 3D geometries for antennas can be fabricated easily in this method as the first step is a 3D printing process.

4.2 Future Work

Several future directions are possible for this work. Improving the resolution of the printing process is a useful direction that can be made possible using techniques like Stimulated Emission Depletion (STED). This can help in the fabrication of even finer antennas. Autofocusing mechanism that can make focusing at a new location of printing easier can be a valuable addition

to this writing mechanism. Detailed study into the mechanism of how antenna and aperture work together, dependence on angle of incidence and how fabrication can be optimized further is another future work direction. Studying complex 3D structures for antennas using this method of fabrication to utilize the full potential of the true 3D printing is also a potential future direction.

REFERENCES

[1] T. Baldacchini, *Three-Dimensional Microfabrication Using Two-photon Polymerization,* Elsevier, (2015).

[2] M. Göppert-Mayer, *Über Elementarakte mit zwei Quantensprüngen,* Ann. Phys. **9,** 273–294, (1931).

[3] S. Wu, J. Serbin, and M. Gu, "Two-photon Polymerization for Three-Dimensional Micro-fabrication," *J. Photochem. Photobiol. A Chem.,* vol. 181, no. 1, pp. 1–11, 2006.

[4] I. Sakellari *et al* "Diffusion-Assisted High-Resolution Direct Femtosecond Laser Writing," *ACS Nano,* vol. 6, no. 3, pp. 2302-2311, 2012.

[5] K. Sugioka and Y. Cheng, "Ultrafast lasers - reliable tools for advanced materials processing," *Light Sci. Appl.*, vol. 3, no. 4, pp. e149–e149, Apr. 2014.

[6] S. Maruo, O. Nakamura, and S. Kawata, "Three-dimensional microfabrication with two-photon-absorbed photopolymerization," *Opt. Lett.*, vol. 22, no. 2, p. 132, 1997.

[7] S. Kawata, H. Sun, T. Tanaka, "Finer features for functional microdevices," *Nature*, vol. 412, no. 1, pp. 697–699, 2001.

[8] C. Schizas *et al.*, "On the design and fabrication by two-photon polymerization of a readily assembled micro-valve," *Int. J. Adv. Manuf. Technol.*, vol. 48, no. 5–8, pp. 435–441, 2010.

[9] A. I. Son *et al.*, "An Implantable Micro-Caged Device for Direct Local Delivery of Agents," *Sci. Rep.*, vol. 7, no. 1, 2017.

[10] X. Zheng *et al.*, "Ultralight, Ultrastiff Mechanical Metamaterials," *Science (80-.).*, vol. 344, no. 6190, pp. 1369–1373, 2014.

[11] H. Nishiyama and Y. Saito, "Electrostatically Tunable Plasmonic Devices using High Order Diffraction Modes on Multi-photon Polymerized Three-dimensional Microsprings," *IEEJ Trans. Sensors Micromachines*, vol. 136, no. 6, pp. 261–265, 2016.

[12] T. Grosjean, M. Mivelle, F. I. Baida, G. W. Burr, and U. C. Fischer, "Diabolo nanoantenna for enhancing and confining the magnetic optical field," *Nano Lett.*, vol. 11, no. 3, pp. 1009–1013, 2011.

[13] R. D. Grober, R. J. Schoelkopf, and D. E. Prober, "Optical antenna: Towards a unity efficiency near-field optical probe," *Appl. Phys. Lett.*, vol. 70, no. 11, pp. 1354–1356, 1997.

[14] P. J. Schuck, D. P. Fromm, A. Sundaramurthy, G. S. Kino, and W. E. Moerner, "Improving

the Mismatch between Light and Nanoscale Objects with Gold Bowtie Nanoantennas," *Phys. Rev. Lett.*, vol. 94, no. 1, p. 17402, Jan. 2005.

[15] L. Wang, S. M. Uppuluri, E. X. Jin, and X. Xu, "Nanolithography Using High Transmission Nanoscale Bowtie Apertures," *Nano Lett.*, vol. 6, no. 3, pp. 361–364, Mar. 2006.

[16] S. A. Maier, *Plasmonics: Fundamentals and applications*. New York, NY: Springer US, 2007.

PUBLICATION

P. Barton, S. Mukherjee, J. Prabha, B. W. Boudouris, L. Pan, and X. Xu, “Fabrication of silver nanostructures using femtosecond laser-induced photoreduction,” *Nanotechnology*, no. 28, 2017.